1. INTRODUCTION

1.1 Presentation

A plunging jet flow is defined as the impingement of a liquid jet into a pool of liquid or a tranquil channel. Classical examples include the vertical plunging jet, the hydraulic jump, a free-falling nappe impacting into a pool (Fig. 1-1). At the intersection of the impinging flow with the receiving body of water, free-surface instabilities develop and air bubble entrainment may be observed (Fig. 1-1 and 1-2). This is a form of local, singular aeration, by opposition to interfacial aeration observed in open channel flows (CHANSON 1997).

Plunging jet flow situations are encountered in Nature : e.g., at the impact of waterfalls (Fig. 1-1A). Industrial applications of plunging jets include minerals-processing flotation cells, waste-water treatment, oxygenation of mammalian-cell bio-reactors and riverine re-oxygenation weirs (e.g. JAMESON 1995, CHANSON 1997, KOLANI et al. 1998) (Fig. 1-1C). In each case a strong mixing process takes place. A related case is the air entrainment by a plunging solid surface in a liquid bath. Such a configuration is used for polymer coating, in the production of photographic film, and it is observed at the impact of a missile with a free-surface (e.g. KNAPP et al. 1970, KENNEDY and BURLEY 1977).

In the oceans, plunging breaking waves can entrain a large amount of air bubbles when the top of the wave forms a water jet projecting ahead of the wave face and impacts the water free-surface in front of the wave (Fig. 1-1B & 6-1). Downstream of the impingement point, the air bubble advective dispersion is a function of the initial jet momentum, pressure gradients, turbulence and currents. Several researchers applied the analogy between plunging jet flows and plunging breakers : e.g., KOGA (1982), GRIFFIN (1984), HUBBARD et al. (1987), CHANSON and CUMMINGS (1994a), CHANSON and LEE (1997), CHANSON et al. (1999). KOGA obtained reasonable results in terms of air entrainment by water droplets re-attaching the free-surface while CHANSON and CUMMINGS predicted re-oxygenation rates of deep-water plunging breakers that were consistent with field observations. CHANSON and LEE showed that the rate of energy dissipation in laboratory plunging breakers are close to the energy dissipation at the plunging jet of drop structures. Most works considered steady plunging jet results obtained with freshwater and there have been suggestions that air entrainment at breaking waves in the Sea might be an entirely different process. For example, the prototype scale is significantly larger than laboratory experiments and fluid properties differ between freshwater and seawater.

1.2 Bibliographic review

Several studies showed that air entrainment at plunging jets takes place when the jet impact velocity exceeds a characteristic velocity V_e which is a function of the inflow conditions (e.g. McKEOGH 1978, CUMMINGS and CHANSON 1999). Some studies, in particular the theses of VAN DE SANDE (1974), McKEOGH (1978), VAN DE DONK (1981), EVANS (1990) and CUMMINGS (1996), contributed significantly to our present understanding of air entrainment/entrapment process at the impingement point.

Fig. 1-1 - Photographs of plunging jet applications

(A) Plunging jet downstream of a water fall : Otodome-no-taki, Shiba river, Japan on 1 Nov. 2001



(B) Plunging breaking wave next to a Surf Life Saving patrol (red and yellow flags) at Narrow Neck, Gold Coast (Australia) on 18 Feb 2001



(C) Plunging jet downstream of Itaipu dam spillway flip bucket, Parana river, Brazil (Courtesy of Itaipu Binacional Corp.) - Flow from right to left



The mechanisms of bubble entrainment depends upon the jet velocity at impact, the physical properties of fluid, the jet nozzle design, the length of free-falling jet and the jet turbulence (BIN 1993). For small jet velocities larger than the onset velocity, air is entrained in the form of individual air bubbles. At larger jet velocities, large packets of air are entrained and broken up subsequently in the shear flow (e.g. BIN 1993, CUMMINGS and CHANSON 1997a, CHANSON and BRATTBERG 1998).

Flow patterns at two-dimensional plunging jet flows were investigated by GOLDRING et al. (1980) and SENE (1988). Recently CUMMINGS and CHANSON (1997a,b), CHANSON and BRATTBERG (1998) and BRATTBERG and CHANSON (1998) presented detailed measurements of air content and velocity distributions below the impingement point.

Several researchers showed interest in circular plunging jets (e.g. reviews by BIN 1993 and CHANSON 1997). Numerous experiments were performed with small circular jets (i.e. less than 5 mm diameter) for which mostly qualitative studies were performed. Only a small number of researchers studied the flow field below impingement. McKEOGH and ERVINE (1981) and VAN DE DONK (1981) recorded air concentration profiles and velocity distributions primarily in the fully-developed flow region; BONETTO and LAHEY (1993) presented results obtained in both developing and fully-developed flow regions; MANASSEH and CHANSON (2001) reported acoustics characteristics of the air entrainment process.

BIN (1993) and CHANSON (1997) highlighted the lack of information on the air content distributions in the vicinity of the impingement point and on the entrained bubble size distributions. Further, physical modelling of

plunging jet flows remains subject to scaling effects which have not properly explained (e.g. WOOD 1991, CHANSON 1997).

1.3 Mechanisms of air entrainment at plunging jets

Air is entrapped/entrained at the impingement perimeter (Fig. 1-2 & 1-3). The entrained air bubbles are carried away within the developing shear flow. After the entrained bubbles lose their downward momentum, some rise freely to the free-surface, giving a 'foamy' appearance to the surrounding fluid. Figures 1-2A and 1-2C show entrained air bubbles in the developing flow region of a vertical circular jet (i.e. $(x-x_1)/r_1 < 15$). Figure 1-2A shows an experiment with seawater while Figure 1-2C presents an experiment in freshwater. Outside of the shear flow, rising bubbles are observed (Fig. 1-2B). Figure 1-2B presents a far view illustrating the downward diffusion region (i.e. white bubbly flow) and surrounding rising bubbles, on the left and right, for the same flow conditions as in Figure 1-2C.

Fig. 1-2 - Photographs of air bubble entrainment at circular plunging jet
(A) Model 4 (d_o = 0.0125 mm, Seawater), x_1 = 0.050 m, V_1 = 2.46 m/s, Fr_1 = 7.2 - Photograph taken with high shutter speed (1/500 s)



(B) Model 2 (d_o = 0.0125 mm, Freshwater), x_1 = 0.050 m, V_1 = 3.45 m/s, Fr_1 = 9.8 - Photograph taken with high shutter speed (1/2,000 s)



(C) Model 2 (d_o = 0.0125 mm, Freshwater), x_1 = 0.050 m, V_1 = 3.45 m/s, Fr_1 = 9.9 - Photograph taken with high shutter speed (1/1,000 s)

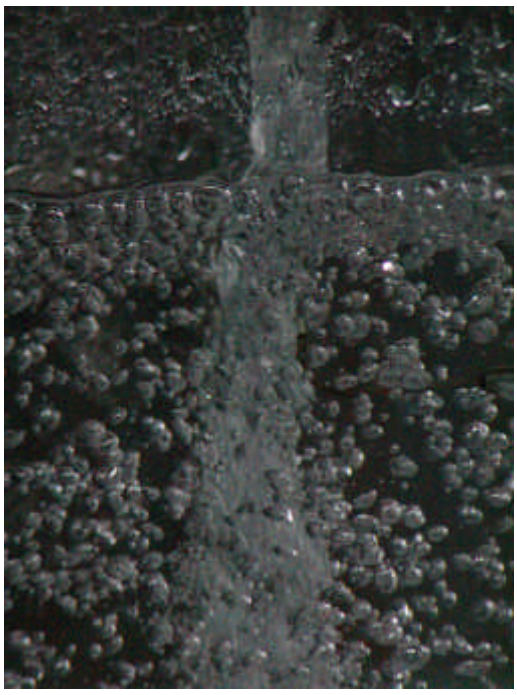
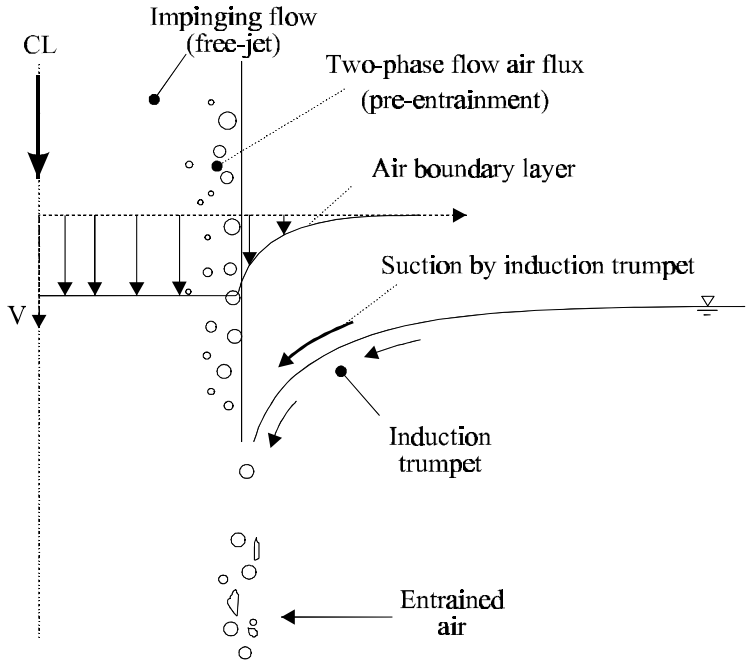


Fig. 1-3 - Mechanisms of air bubble entrapment at the impingement perimeter of a vertical plunging jet (after CHANSON 1997)



Air entrainment at impingement may occur by three different mechanisms : i.e, two-phase flow air flux, entrapment of the air boundary layer and suction (aspiration) at the induction trumpet (CHANSON 1997) (Fig. 1-3). If the impinging jet is aerated, upstream of the intersection with the pool of water, the flow aeration at the inflow free-surface is entrained past the impingement point. This process is also called pre-entrainment or two-phase flow air flux. Secondly air is entrained by shear friction near the free-surface of the impinging flow (i.e. the air boundary layer) and some air may be trapped also at the entrainment point. The third mechanism is the aspiration or suction of the induction trumpet (Fig. 1-3). At the closure of the trumpet, air packets are entrapped and entrained within the shear flow. CHANSON and BRATTBERG (1998) discussed specifically the properties of the induction trumpet and the re-analysis of their results showed that aspiration at induction trumpet accounted for most entrained air in their experiments. During the present study, the free-falling jet was clear, non-aerated and the jet surface roughness appeared very small suggesting that air entrapment at the induction trumpet was the dominant entrainment mechanism for the range of investigated jet diameters, velocity and length (Table 2-1).

1.4 Dimensional analysis and similitude

Analytical and numerical studies of the air entrapment and diffusion processes are complex because of the large number of relevant equations. Experimental investigations are often preferred and this study is no exception. Laboratory studies of air-water flows require however the selection of an adequate similitude.

Considering air bubble entrainment at vertical plunging water jets, the relevant parameters needed for any dimensional analysis include :

- the fluid properties and physical constants; these consist of the pressure above the flow P_{atm} (Pa), the temperature of air and water (K), the density of water ρ_w (kg/m^3), the density of air ρ_{air} (kg/m^3), the dynamic viscosity of water μ_w (N.s/m^2), the dynamic viscosity of air μ_{air} (N.s/m^2), the surface tension of air and water σ (N/m), the vapour pressure at the experiment temperature P_v (Pa), and the acceleration of gravity g (m/s^2);
- the channel (or flow) geometry; that is, the channel width W (m);
- the upstream flow properties; these are the free-jet length x_1 (m), the upstream velocity V_1 (m/s), the inflow jet diameter d_1 (m), the upstream air concentration distribution, the upstream profiles of longitudinal and lateral components of the turbulent velocity fluctuations;
- the air-water flow properties; these consist of the distributions of void fraction and velocity, the distributions of axial and lateral components of the turbulent velocity fluctuations, the distributions of entrained bubble sizes at each location (x, y).

The above analysis may be simplified. Usually the air pressure is atmospheric and when the vapour pressure is small compared to the atmospheric pressure, the parameters P_{atm} and P_v may be neglected. In addition compressibility effects are ignored. When the local void fraction C is known, the density and viscosity of the air-water mixture can be deduced as $\rho_w*(1 - C)$ and $\mu_w*(1 + 2.5*C)$ respectively and the parameters ρ_{air} and μ_{air} can be ignored. At atmospheric pressure and for a constant temperature, the air and water fluid properties (i.e. ρ_w, μ_w, σ) are constants for a given set of fluids (e.g. air and freshwater).

Normally the distributions of air-water flow parameters are replaced by a characteristic value : e.g., a characteristic flow velocity V (m/s), a characteristic void fraction C, and the root mean square of axial and transverse components of turbulent velocity u' and v' (m/s). For axi-symmetrical water jets ERVINE and FALVEY (1987) showed that the lateral component of turbulence intensity v'/V is proportional to the axial turbulence intensity u'/V. Such a relationship enables u' and v' to be replaced by the single independent parameter u'. The distributions of bubble sizes may be replaced by a characteristic bubble size d_{ab} (m).

The air flow rate can be deduced by continuity from the air concentration and velocity distributions or from the air bubble size distribution. It is not an independent parameter. Similarly the bubble count rate is a function of the void fraction, velocity and bubble size : it is not independent.

Taking into account all the above parameters, dimensional analysis yields :

$$F_1(\rho_w, \mu_w, \sigma, g, W, V, C, u', d_{ab}, x, y, x_1, V_1, d_1, (u')_1, \ ...) \ = \ 0 \qquad (1\text{-}1)$$

The above variables give the following dimensionless numbers : the characteristic void fraction C or the non-dimensional air flow rate Q_{air}/Q_w, the dimensionless geometric variables W/d_1, the Froude number $Fr = V/\sqrt{g * d_1}$, the turbulence intensity $Tu = u'/V_1$, a dimensionless characteristic bubble size d_{ab}/d_1. The dimensionless inflow variables are $Fr_1 = V_1/\sqrt{g * d_1}$, $Re_1 = \rho_w*V_1*d_1/\mu_w$, $We_1 = \rho_w*V_1^2*d_1/\sigma$, $Tu_1 = (u')_1/V_1$ where Fr_1, Re_1 and We_1 are Froude, Reynolds and Weber numbers respectively. Any combination of these numbers is dimensionless and may be used to replace one of the combinations. For example, one dimensionless inflow parameter may be replaced by the Morton number $Mo = (g*\mu_w^4)/(\rho_w*\sigma^3)$, also called liquid parameter, since :

$$Mo \ = \ \frac{We_1^3}{Fr_1^2 * Re_1^4} \qquad (1\text{-}2)$$

The Morton number is a function of fluid properties and gravity constant. For the same fluids (e.g. air and water) in both model and prototype, the Morton number is a constant.

If the sidewall effects are assumed small, the channel width may be neglected. From these considerations the relationship (1-1) becomes in terms of dimensionless parameters :

$$F_2\left(C ; Fr ; Tu ; \frac{d_{ab}}{d_1} ; \frac{x - x_1}{d_1} ; \frac{y}{d_1} ; \frac{x_1}{d_1} ; Fr_1 ; We_1 ; Tu_1 ; Mo \right) = 0 \qquad (1\text{-}3)$$

In Equation (1-3), C, Fr, Tu and d_{ab}/d_1 are dimensionless characteristics of the flow field below impingement at a location $\{(x\text{-}x_1)/d_1, y/d_1\}$ while x_1/d_1, Fr_1, We_1, Tu_1 and Mo characterise the inflow conditions and fluid properties.

In free-surface flows, gravity effects are important and most laboratory studies are based upon a Froude similitude (e.g. HENDERSON 1966, HUGHES 1993, CHANSON 1999). That is, the Froude number must be identical in model and prototype. The entrapment of air bubbles and the mechanisms of air bubble breakup and coalescence are dominated by surface tension effects implying the need for Weber similitude. For geometrically-similar models, it is impossible to satisfy simultaneously Froude and Weber similarities. In small size models based upon a Froude similitude, the air entrainment process may be affected by significant scale effects : i.e., small model flows entrain less if no air compared to prototype flows. WOOD (1991) and CHANSON (1997) presented comprehensive reviews. KOBUS (1984) presented some applications.

1.4 Structure of the report

In the present work, the writers investigated experimentally air entrainment and bubble dispersion at vertical circular plunging jets. Three geometric scales were selected and similar experiments were conducted based upon a Froude similitude. That is, detailed air-water measurements were performed systematically for identical Froude numbers. For one geometric scale, identical experiments were reproduced with freshwater, seawater and salty freshwater. The results contribute to a better understanding of air entrainment at vertical circular plunging jets and of the differences in air entrainment mechanisms between freshwater, salty water and seawater. Basic design recommendations are presented to ensure minimum scale effects.

Calculations of bubble rise velocity are detailed in Appendix A. Void fraction, bubble count rate and bubble chord time results are presented in Appendices B and C. Composition of the salty freshwater solution is given in Appendix D and compared with seawater composition.

2. EXPERIMENTAL FACILITIES

2.1 Experimental channels

Experiments in circular plunging jet flows were conducted in two flumes with five configurations called Models 1, 2, 3, 4 and 5 (Table 2-1, Fig. 2-1 & 2-2). Experiments with Models 1, 2 and 3 were conducted with freshwater. Experiments with Models 4 and 5 were performed with seawater and salty freshwater respectively.

Model 1 was located at the University of Queensland, Australia. The receiving channel was 0.3 m wide, 3.6 m long and 1.8 m deep with glass walls (10-mm thick). The circular nozzle was made of aluminium with a 1/2.16 contraction ratio (elliptical profile) and located at the end of a 3.5 m long circular PVC pipe (Fig. 2-1A & 2-2A). Models 2, 3, 4 and 5 were located at Toyohashi University of Technology, Japan. The receiving flume was 0.10 m wide, 0.75 m deep and 2 m long. The nozzle was sharp-edged, being machined with an accuracy less than 0.1 mm and the water was supplied by a straight circular vertical PVC pipe (Fig. 2-1B & 2-2B).

The Models were designed to be geometrically similar based upon a Froude similitude with undistorted scale (e.g. HUGHES 1993, CHANSON 1999). The geometric scaling ratio was L_R = 2.0 between Model 1 and Models 2, 4 and 5, and L_R = 3.66 between Models 1 and 3. Similar experiments were conducted for identical Froude numbers $Fr_1 = V_1/\sqrt{g*d_1}$ where V_1 is the jet impact velocity, g is the gravity constant and d_1 is the jet diameter at impingement. Measurements were performed at similar cross-sections $(x-x_1)/r_1$ where x is the longitudinal coordinate, x_1 is the free jet length and r_1 is the jet impact radius : i.e., $r_1 = d_1/2$ (Fig. 2-1).

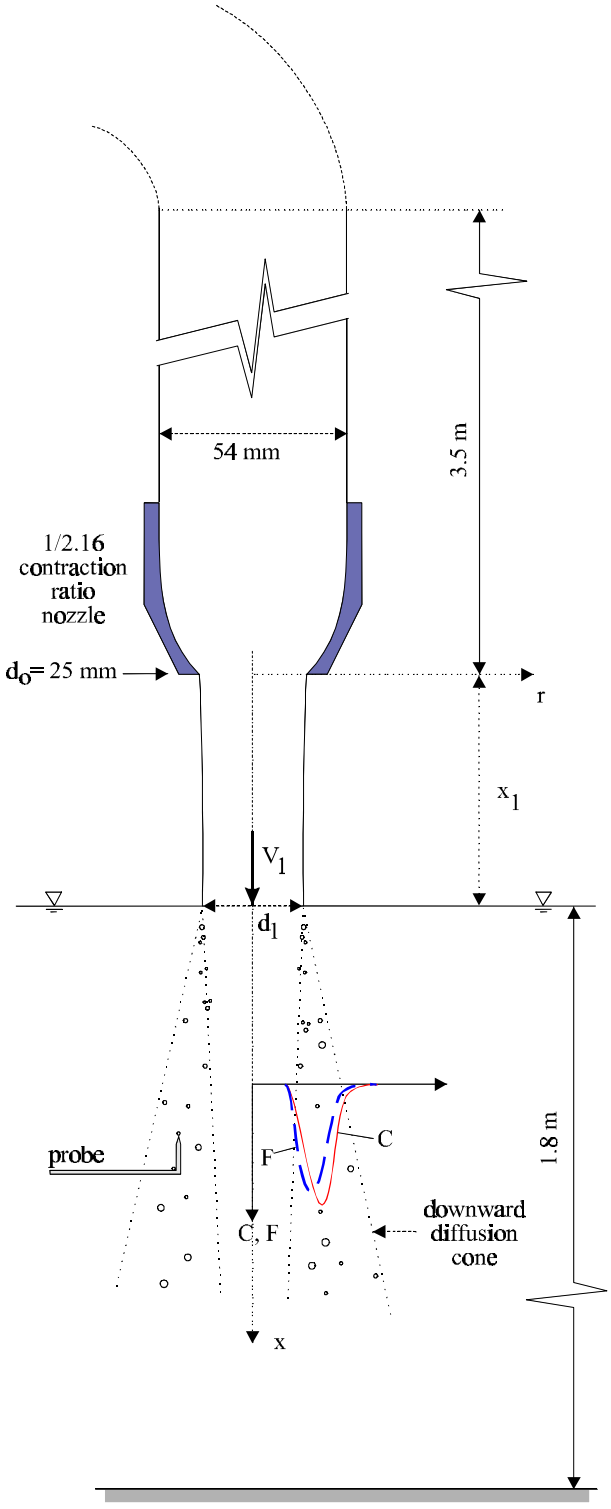
Table 2-1- Summary of experimental flow conditions

Ref.	d_o	x_1 [a]	V_1	Fr_1	Tu_1	Run number	Comments
	m	m	m/s	m			
(1)	(2)	(3)	(4)	(5)	(6)	(7)	(8)
Model 1	0.025	0.1	3.5	7.2	0.39%	BM35_1	Freshwater (tap water, σ = 0.055 N/m). Vertical jet. Inflow pipe: 3.5 m long, 0.054 m diameter. Water depth: ~1.5 m.
			4.1	8.4	0.46%	BM4_2	
			4.4	9.0	0.96%	BM44_2	
Model 2	0.0125	0.05	2.42	7.1	N/A	Cir_2	Freshwater (tap water, σ = 0.073 N/m). Vertical jet. Inflow pipe: 1.2 m long, 0.0125 m diameter. Water depth: ~0.65 m.
			3.04	8.8		Cir_4	
			3.18	9.2		Cir_5	
			3.46	10.0		Cir_6	
Model 3	0.00683	0.0273	1.79	7.1	N/A	Run_1	Freshwater (tap water, σ = 0.073 N/m). Vertical jet. Inflow pipe: 1 m long, 0.00683 m diameter. Water depth: ~0.65 m.
			2.16	8.5		Run_2	
			2.30	9.0		Run_3	
			2.49	9.7		Run_4	
Model 4	0.0125	0.05	2.46	7.2	N/A	Sea_2	Seawater (Pacific Ocean, σ = 0.076 N/m). Vertical jet. Inflow pipe: 1.2 m long, 0.0125 m diameter. Water depth: ~0.65 m.
			2.87	8.3		Sea_4	
			3.13	9.1		Sea_5	
			3.36	9.7		Sea_6	
Model 5	0.0125	0.05	3.12	9.0	N/A	Salt_5	Freshwater with 34.5 ppt NaCl (99.5% quality) (σ = 0.075 N/m). Vertical jet. Inflow pipe: 1.2 m long, 0.0125 m diameter. Water depth: ~0.65 m.

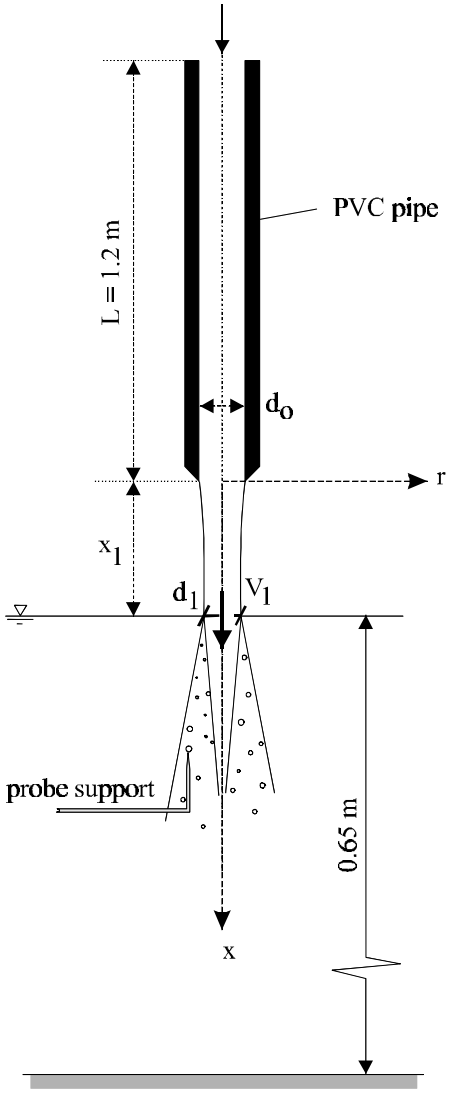
Notes : Tu_1 : turbulence intensity of the jet core at impact; σ : measured surface tension between air and water; ([a]) : longitudinal distance between the nozzle and the free-surface pool; N/A: information not available.

Fig. 2-1 - Sketch of the experimental facilities

(A) Model 1



(B) Models 2, 3, 4 and 5



2.2 Instrumentation

In Model 1, the discharge was measured with an orifice meter (British Standards design) calibrated on-site with a volume-per-time technique. The flow rate was measured with a volume per time technique in Models 2, 3, 4 and 5. The error on the discharge measurement was less than 2%.

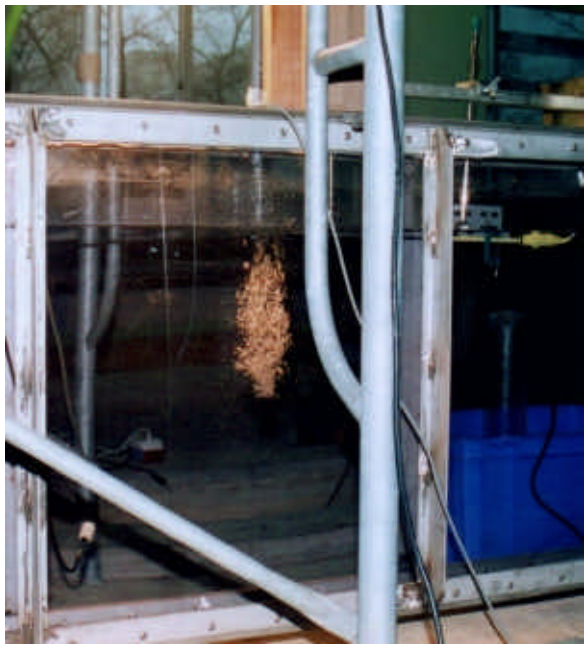
In the largest facility (Model 1), clear water jet velocities and turbulent velocity fluctuations were measured in the free-falling jet using a Prandtl-Pitot tube (diameter 3.3 mm) and a conical hot-film probe system. The Prandtl-Pitot tube was connected to a Validyne pressure transducer scanned at 500 Hz. The miniature hot-film probe (Dantec 55R42, 0.3 mm size) was scanned at 40 kHz. It was initially calibrated with the Pitot tube data and the velocity distribution was checked with the measured flow rate (within 2%) for jet velocities ranging from 1 to 5 m/s.

Fig. 2-2 Photographs of the experimental flumes

(A) Model 1 (d_o = 0.025 m, Freshwater), x_1 = 0.10 m, V_1 = 3.3 m/s, Fr_1 = 6.8



(B) Model 2 (d_o = 0.0125 m, Freshwater), x_1 = 0.0935 m, V_1 = 1.96 m/s, Fr_1 = 6.1



Air-water flow properties were measured with single-tip conductivity probes (needle probe design) (Fig. 2-5B). In Model 1, the probe consisted of a sharpened rod (platinum wire ∅ = 0.35 mm) which was insulated except

for its tip and set into a metal supporting tube (stainless steel surgical needle ∅ = 1.42 mm) acting as the second electrode. The probe was excited by an electronics (Ref. AS25240) designed with a response time less than 10 μs and calibrated with a square wave generator. Further details on the probe design and electronic system were reported by CHANSON (1995) and CUMMINGS (1996). During the present study, the probe output signal was scanned at 5 kHz for three minutes.

A Kanomax™ System 7931 resistivity probe (inner electrode ∅ = 0.1 mm) was used in Models 2, 3, 4 and 5. The electronics had a response time estimated to be less than 30 μs ([1]). The void fraction and bubble count rate were calculated by the Kanomax™ analog integrator during five minutes in Models 2 and 3. With seawater (Model 4) and salty freshwater (Model 5), probe contamination was experienced and the analog signal was integrated for 40 seconds only. In Models 2, 4 and 5, raw probe outputs were recorded at 25 kHz for 2.6 seconds to calculate bubble chord time distributions.

Conductivity probe measurements were taken on the jet diameter through the centreline. In each Model and at each cross-section, the probe sensor and support were initially located at $r < -2*r_1$ and measurements were conducted by moving the probe tip with increasing radial coordinate r up to over $r > +2*r_1$ where r_1 is the jet impact radius (Fig. 2-1). The displacement of the probes in the flow direction and direction normal to the jet support was controlled by fine adjustment travelling mechanisms. The error in the probe position was less than 0.2 mm in each direction. Additional measurements were performed using high speed photographs and movies. Underwater acoustics were measured in Model 1 and results were reported by CHANSON and MANASSEH (2000, Internet resource) and MANASSEH and CHANSON (2001).

Water density was measured with a Nagashima™ Standard Hydrometer GI-0361-11. Dynamic viscosity was measured with a cone and plate viscosimeter Toki™ RE80 operated at controlled temperature. Kinematic viscosity was measured with a capillary master viscosimeter Sibata™ SU-898 (model SU-93309). Surface tension was recorded using a surface wave method (e.g. IINO et al. 1985).

2.3 Physical properties

The experiments were performed at ambient conditions : i.e., atmospheric air was the gas phase. The liquid solution was either freshwater, seawater or salty freshwater. In Models 1, 2 and 3, freshwater (tap water) was used. Water was changed after each experiment. Model 4 experiments were performed with ocean water. Seawater was collected on the Enshu coast (Pacific Ocean, Fig. ii) off the breakers by a group of surfers (Fig. 2-3). The collected waters were transparent and coarse suspended sediment material was filtered prior to the experiment. Seawater experiments were conducted within 3 days of seawater collection ([2]). Model 5 experiments were conducted with salty freshwater. The water solution was made of tap water ([3]) plus 3.45% per weight of sodium chloride (NaCl) with a 99.5% quality (App. D).

---

[1] Kanomax™ did not give a response time and indicated that the electronics had a time constant of 1,500 μs. The writers estimated the response time (less than 30 μs) based upon their experience during the present study.

[2] The experience of the second author suggests that seawater may be considered "fresh" up to 3 days after collection. Afterwards plankton deceases.

[3] as in Models 2 and 3.

Physical properties of tap water, seawater and salty freshwater were measured in the Chemical and Mechanical Engineering Departments. The results (Table 2-2) are consistent with those reported by RILEY and SKIRROW (1965). Seawater properties were recorded before and after each experiment. (Seawater had a clear appearance at collection, as well as after three days of experiments.)

Remarks

Density, viscosity and surface tension differed little between the three water solutions and the Morton number ranged from 3.5E-7 to 1E-6 (Table 2-2).

Preliminary tests showed that the flume had to be carefully cleaned before each seawater experiment to avoid pigmentation and flocculation. When the flume was not properly cleaned, flocs could be detected after about 2-3 hours of experiments. Figure 2-4 presents a microscope photograph of seawater residue screened with a 0.45 micron filter. It is believed that rust oxidation at the bottom of the stainless channel caused the flocs during plunging jet operation. All seawater experiments were conducted after flume cleaning prior to the start of each experiment.

Fig. 2-3 - Seawater collection

(A) Surfers (black dots) on their way to collect seawater off the breakers at Terasawa beach on 22 Oct. 2001



(B) Check of seawater containers on Terasawa beach on 25 Oct. 2001 by Dr AOKI (right, green jacket) and Dr CHANSON (left, black shorts)



Fig. 2-4 - Microscope photograph of seawater residue (0.45 micron filter) and dead plankton during preliminary tests (Model 4)

The TV screen width (25-cm real size) corresponds to about 100 microns at full scale. Residue was probably caused by rust oxidation. After careful cleaning of the flume, no further flocculation was observed.

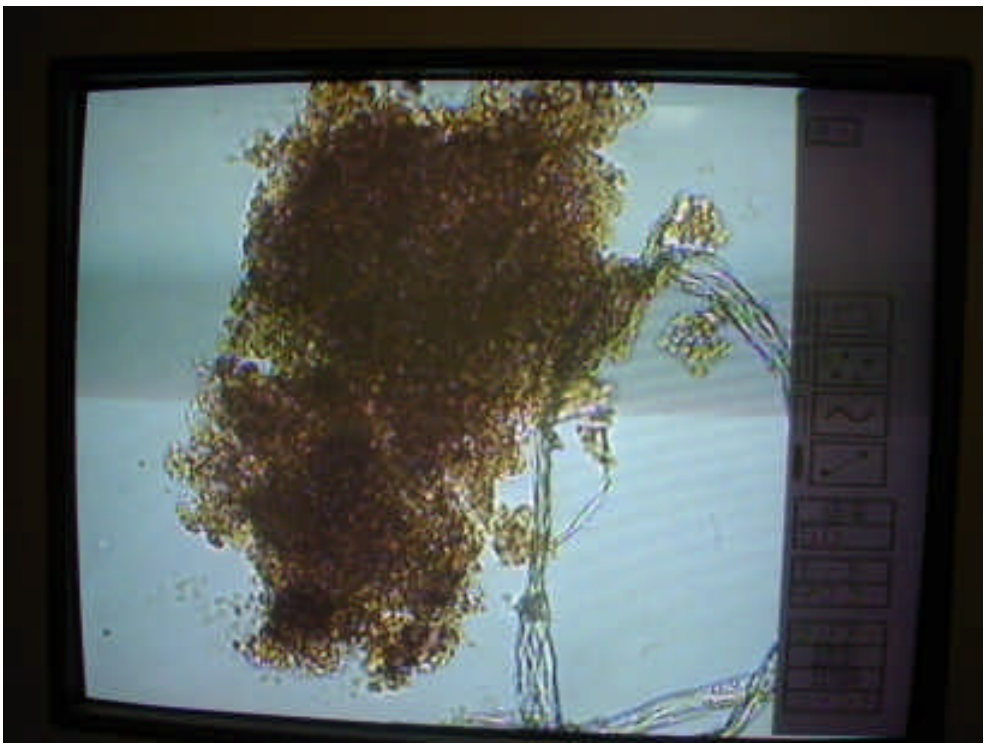


Table 2-2- Measured physical properties of water

Property	Tap water	Seawater (new, after collection)	Seawater (old, after experiment)	Salty tap water (3.45% solution)	Remarks
(1)	(2)	(3)	(4)	(5)	(6)
Experiments :	Models 1, 2 & 3	Model 4	Model 4	Model 5	See Table 2-1.
Density (kg/m^3) :	998.2	1,024	1,023	1,024	At 20 Celsius.
Dynamic viscosity (Pa.s):	1.015 E-3	1.22 E-3	1.24 E-3	1.18 E-3	At 20 Celsius.
Kinematic viscosity (m^2/s):	0.925 E-6	0.971 E-6	0.963 E-6	0.962 E-6	At room temperature (about 22 Celsius).
Surface tension (N/m):	0.075 (Models 2 & 3) 0.055 (Model 1)	0.076	--	0.075	At room temperature (about 22 Celsius).
Conductivity (μS/cm):	87.7	48,500 49,100	48,500	53,600	At 25 Celsius.
pH :	6.83	-- 8.12	7.68	6.94	At room temperature (about 22 Celsius).
Dissolved oxygen (ppm):	--	-- 8.7	--	--	At room temperature (about 21 Celsius).
Dissolved oxygen (%):	--	-- 100%	100%	--	
Morton number Mo :	3.5 E-7 (Models 2 & 3) 1.1 E-6 (Model 1)	5.5 E-7	--	5.0 E-7	$Mo = \frac{g * \mu_w^4}{\rho_w * \sigma^3}$

2.4 Data processing

The measurement principle of conductivity probes is based upon the difference in electrical resistivity between air and water. The resistance of water is one thousand times lower than the resistance of air bubbles. When the probe tip is in contact with water, current will flow between the tip and the supporting metal; when it is in contact with air no current will flow. Typical probe signals are shown in Figure 2-5 for Models 2 and 4. A sketch of single-tip conductivity probe is presented in Figure 2-5B. In Figure 2-5A, the water voltage is about +0.2 V and +0.85 V for freshwater and seawater respectively. Each steep rise of the signal corresponds to an air bubble pierced by the probe tip. Although the signal is theoretically rectangular, the probe response is not square because of the finite size of the tip, the wetting/drying time of the interface covering the tip and the response time of the probe and electronics.

The air concentration or void fraction C is the proportion of time that the probe tip is in the air. Past experience showed that the probe orientation with the flow direction has little effect on the void fraction accuracy provided that the probe support does not affect the flow past the tip (e.g. SENE 1984, CHANSON 1988). This was true in Model 1 but the Kanomax™ resistivity probe was possibly affected by the probe orientation (YASUDA 2001,

Personal communication). In the present study, the probe tip was aligned with the flow direction as sketched in Figure 2-5B.

The bubble count rate F is the number of bubbles impacting the probe tip. The measurement is sensitive to the probe tip size, bubble sizes, velocity and discrimination technique, particularly when the sensor size is larger than the smallest bubble sizes. Note that there is a relationship between bubble count rate and void fraction as demonstrated by TOOMBES (2002) but it is not unique in the developing region of plunging jet flows (BRATTBERG and CHANSON 1998).

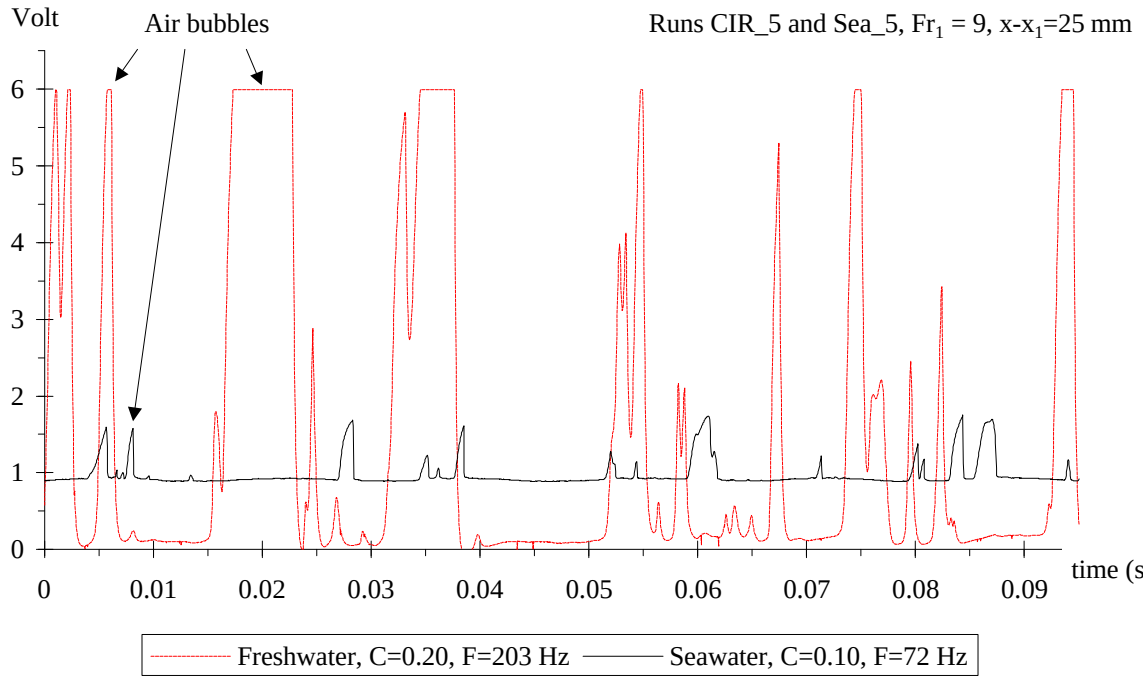
Fig. 2-5 - Single-tip conductivity probe response in bubbly flows

(A) Raw probe signals (Kanomax™ probe output) in seawater and freshwater, scanned at 25 kHz

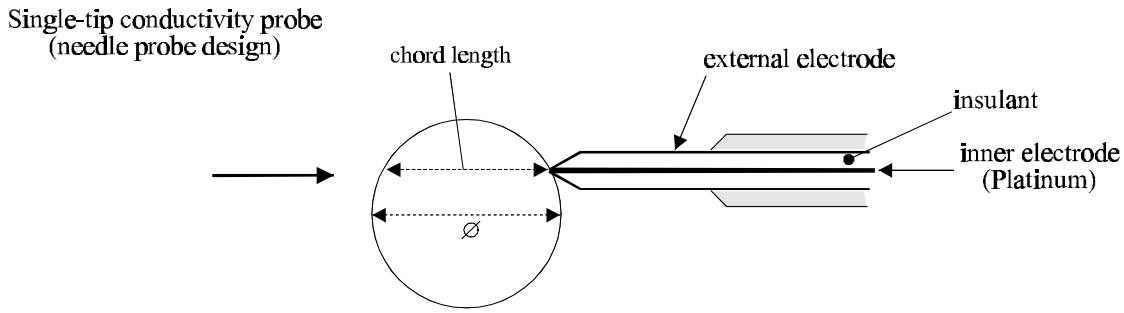
Freshwater data : Run Cir_5, Fr_1 = 9.2, x_1 = 0.05 m, x-x_1 = 0.025 m, C = 0.20, F = 203 Hz, r > 0

Seawater data : Run Sea_5, Fr_1 = 9.1, x_1 = 0.05 m, x-x_1 = 0.025 m, C = 0.10, F = 72 Hz, r > 0

In both cases, the electronics gain was maximum but different bias were set



(B) Sketch of single-tip conductivity probe sensor



The bubble chord time is defined as the time spent by the bubble on the probe tip. In Models 2, 3, 4 and 5, bubble chord times were calculated from the raw probe signal scanned at 25 kHz for 2.6 seconds at eight different locations, per cross-section, selected next to the location of maximum void fraction and maximum bubble frequency. The signal was processed using a single threshold technique and the threshold was set at about 15-20% of the air-water voltage range. (An incomplete sensitivity analysis was conducted with thresholds between 10 and 30% of the voltage range. The results showed little effect of the threshold on chord time results. Time-variations of the water voltage during the scan period (i.e. 2.6 sec.) was a problem however and some data sets had to be rejected when the water voltage variations exceeded 10% of the air-water voltage range during a scan.)

The complete set of experimental data is presented in Appendices B and C for void fraction and bubble count rate, and bubble chord time respectively.

2.5 Discussion

Air-water measurement accuracy and differences between resistivity probes

The data accuracy was typically $\Delta C/C < 2\%$ for void fractions above 2% and velocities larger than 0.5 m/s. The smallest detectable chord length size was about 0.35 mm with the Model 1 resistivity probe and 0.1 mm with the Kanomax probe (Models 2, 3, 4 & 5) for the investigated flow conditions (i.e. V ~ 1 to 6 m/s). The accuracy on bubble count rate is a function of the bubble size distributions. In the present study, the mean bubble size was about one order of magnitude greater than the probe sensors and the accuracy on bubble count rate was about $\Delta F/F < 5\%$.

Differences were expected between the two resistivity probe systems because of different probe design, sensor size and electronics. While it is difficult to quantify these differences, the experience gained during the experiments suggested that :

- the Kanomax™ probe was able to detect very-fine bubbles (possibly less than 0.1 mm chord size) when the electronics setup was optimum;
- the air bubble detector Ref. AS25240 (Model 1) had a faster response time than the Kanomax™ system and it was easier to setup;
- the Model 1 probe was more robust than the Kanomax™ probe; its lifetime was more than 10 times greater than a Kanomax™ probe lifetime; in one case, the Model 1 probe was repaired on site ([4]);
- the Kanomax™ electronics setup was difficult in seawater (see below).

Resistivity probe operation in seawater and salty freshwater

Only the Kanomax™ System 7931 resistivity probe was used in seawater (Model 4) and salty freshwater (Model 5); the following comments are limited to this system. The probe was designed to operate in freshwater and the manufacturer guaranteed its operation in seawater and in salty water. In practice, some difficulty was experienced.

[4]The Kanomax™ probe cannot be replaced and it had to be completely replaced once.

Although seawater is about 500 times more conductive than tap water (Table 2-2), the probe output was about 4 to 10 times smaller in seawater (Model 4) than the freshwater probe output. For example, in Figure 2-5, the air-water voltage range is about 10 times less in seawater than in freshwater. In salty freshwater (Model 5), the air-water voltage range was about 1.5 to 2 times larger than in seawater, although still 2 to 5 times less than in freshwater.

Contamination of the probe sensor was observed after 2-3 hours of continuous operation in seawater (Model 4). In some cases, the probe tip could be cleaned by placing the probe in a bubbly column of freshwater for 5-10 minutes. In more severe situations, the probe tip and the probe holder had to be cleaned with pure alcohol and tested again in freshwater bubbly flow. No such contamination was experienced in salty freshwater nor in freshwater.

During the experiments, time-variations of the water voltage were experienced with all water solutions : i.e., in freshwater, seawater and salty freshwater. The problem was more acute in seawater because of the small air-water voltage range (e.g. Fig. 2-5). The probe output signal was continuously monitored and the Kanomax™ electronics bias had to be adjusted manually at regular intervals outside of scan periods. (The electronics was never adjusted during data recording and data sets were discarded when significant water voltage shifts were noted during the scan. Recalibration of the electronics was regularly conducted in a bubbly column of freshwater of known void fractions.)

Remarks

It is possible that the small air-water voltage range, observed in seawater, could lead to greater data error in seawater than in freshwater. Specifically the non-detection of small bubbles could lead to inaccurate, biased void fraction and bubble count rate data. Preliminary tests were conducted in a bubbly seawater column of known void fraction and showed that millimetric bubbles were properly accounted for. Tests in plunging jet flows highlighted also that bubbles smaller than 0.1 mm could be detected in seawater when the electronics setup was optimum. The writers believe that, during the seawater experiments, the largest bubbles, which account for the bulk of the void fraction, were properly detected and that the void fraction data were accurate. It is however possible that some fine bubbles (i.e. sizes less than 0.5 mm) were not always detected by the Kanomax™ electronics and the writers acknowledge that bubble count rate data in seawater might underestimate the real numbers of bubbles.

3. EXPERIMENTAL RESULTS. (1) BASIC FLOW PATTERNS

3.1 Inception of air bubble entrainment

At the impact of a plunging liquid jet with a receiving pool, air bubbles may be entrained if the impact velocity V_1 exceeds a critical velocity V_e, called onset velocity or inception velocity. The present results of air entrainment inception conditions are summarised in Table 3-1, where the onset velocity for air entrainment V_e is defined as the mean jet velocity at impact, Tu_1 is the jet turbulence intensity at impact, d_1 is the jet thickness at impact and x_1 is the length of the free-falling jet. In Model 3 (d_o = 6.8 mm), the jet inflow conditions at inception were laminar ([5]) and not strictly comparable with the larger Models.

Inception of air bubble entrainment is not a precise condition (CUMMINGS and CHANSON 1999). For example, entrainment of bubbles of less than 0.2 mm diameter is very difficult to detect visually. Further a jet may entrain one or a few bubbles only every few minutes and the selection of the investigation period is critical. In Model 1 (d_o = 25 mm), "*inception*" was defined as the flow conditions for which one bubble was entrained during a 1 minute period, in the absence of bubbles in the plunge pool. In the smaller flumes (Models 2, 3, 4 & 5), a longer investigation period was selected because of occasional entrapment of fine bubbles : "*inception*" was defined when less than three bubbles were entrained during a 3 minutes period, in the absence of bubbles in the plunge pool.

McKEOGH (1978) showed first that the inception conditions are functions of the free-falling jet turbulence : i.e., V_e = f(Tu). CUMMINGS and CHANSON (1999) re-analysed a large number of experimental data obtained in two-dimensional and circular jets. Their analysis is presented in Figure 3-1 where the experimental observations for Model 1 were added. The data indicate a decreasing inception velocity with increasing turbulence level and a limit V_e = 0.8 m/s for large turbulence levels. The Model 1 data are consistent with the trend (Fig. 3-1).

Although jet turbulence was not measured in Models 2, 3, 4 & 5, the inception results (i.e. V_e = 0.5 to 1.5 m/s) are consistent with the observations of McKEOGH (1978) and ERVINE et al. (1980). They demonstrate also that the inception conditions are identical in freshwater, seawater and salty freshwater for an identical experiment : i.e., V_e = 1.0 m/s for d_o = 12.5 mm and x_1 = 50 mm (Table 3-1). It was observed consistently that the inception velocity V_e increased with increasing jet length x_1 for a given experiment. Such a result contradicts apparently suggestions of decreasing inception velocity for large jet lengths ([6]). During the present study, the jet length was relatively short (i.e. $x_1/d_o < 8$). Visual observations showed a rapid jet contraction with increasing distance x_1 and increasing jet velocity V_1. It is hypothesised that the jet contraction led to a damping of jet turbulence and hence an increase in inception velocity consistent with the experimental trend illustrated in Figure 3-1.

---

[5]Visually the free jet surface was smooth followed by free-surface annular waves similar to wavy flow patterns illustrated by BRENNEN (1970), HOYT and TAYLOR (1977) and CHANSON (1997).

[6]For example, the concept of free-jet pre-aeration (VAN DE SANDE and SMITH 1973) or the concept of free jet surface roughness (e.g. ZHU et al. 2000)

Table 3-1 - Inception of air bubble entrainment : experimental observations in vertical circular plunging jets

Ref.	V_e m/s	Tu_1	d_1 m	x_1 m	Fluid	Inception definition	Remarks
(1)	(2)	(3)	(4)	(5)	(6)	(7)	(8)
Model 1					Tap water	Less than 1 bubble during 60 sec.	d_o = 25 mm.
	0.5225	0.0116	0.0224	0.005			
	0.874	0.00984	0.0200	0.023			
	1.583	0.00468	0.0171	0.100			
	2.102	0.0040	0.0145	0.200			
Model 2					Tap water	Less than 3 bubbles during 180 sec.	d_o = 12.5 mm.
	0.748	--	0.0074	0.025			
	1.027	--	0.0064	0.050			
	1.419	--	0.0050	0.100			
Model 3					Tap water	Less than 3 bubbles during 180 sec.	d_o = 6.83 mm.
	<u>0.523</u>	--	0.00242	0.0137			Laminar inflow conditions.
	0.735	--	0.00204	0.0273			
	1.038	--	0.00172	0.0547			
Model 4					Seawater	Less than 3 bubbles during 180 sec.	d_o = 12.5 mm.
	1.035	--	0.00672	0.050			Prior to plunging jet experiment.
	1.051	--	0.00723	0.0505			After experiment (with flocculation).
Model 5					Salty freshwater	Less than 3 bubbles during 180 sec.	d_o = 12.5 mm.
	1.000	--	0.0046	0.050			

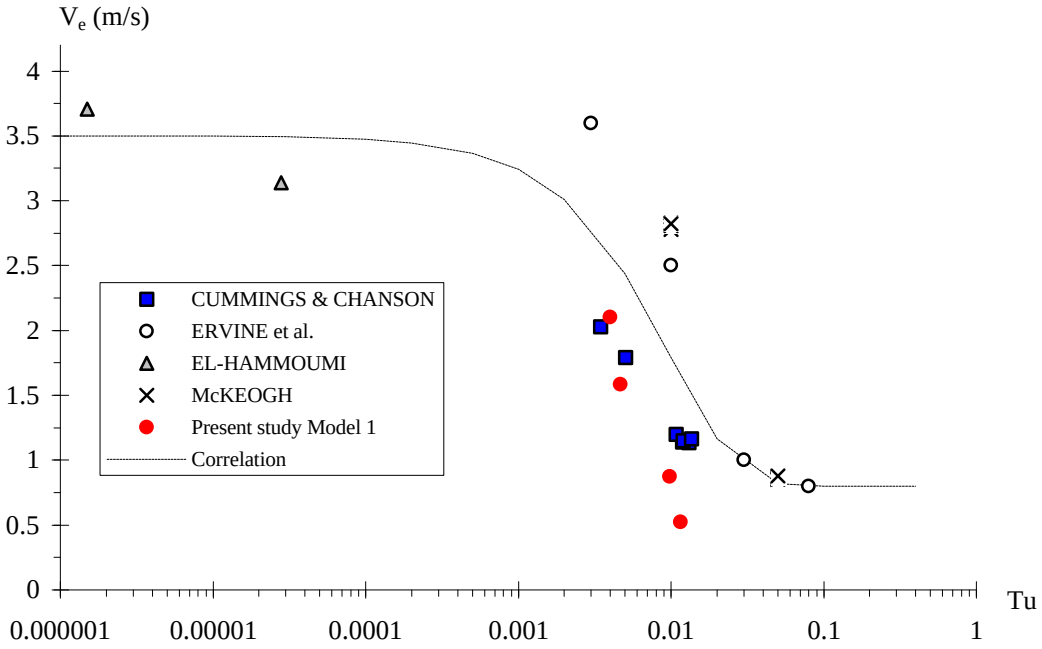
Notes : <u>underlined data</u> : laminar inflow conditions; V_e : jet velocity at impact; Tu_1 : jet centreline turbulence intensity at impact; (--) : information not available.

3.2 Air-water flow patterns

Each model exhibited similar flow patterns although some features were best observed in the largest experiment Model 1 (Fig. 3-2). For all experiments, the free jet was transparent up to impingement. No entrained bubbles were seen in the jet although some small longitudinal streaks were visible at the free-surface. For $V_1 > V_e$, air entrainment was visible and Figure 3-2 presents four underwater photographs of the bubbly flow region in freshwater (Fig. 3-2A & 3-2B), salty freshwater (Fig. 3-2D) and seawater (Fig. 3-2C).

For a jet velocity slightly greater than the inception velocity, individual air bubble entrainment was observed as illustrated in Figure 3-2A. Most entrapped bubbles were visually small : i.e., with diameter less than 0.5 to 1 mm. Although some bubble trajectories were vertical, most entrained bubbles tended to follow a slightly helicoidal trajectory around the jet centreline.

Fig. 3-1 - Inception velocity as a function of jet turbulence at vertical plunging water jets
Two-dimensional plunging jets : CUMMINGS and CHANSON (1999) - Circular plunging jets : McKEOGH (1978), ERVINE et al. (1980), EL-HAMMOUMI (1994), Present study (Model 1)



For larger jet velocities ($V_1 > V_e$), an unstable air cavity developed at one point along the impingement perimeter. The air cavity position changed with time in an apparently random manner. Larger air packets were entrained below the air cavity with the stretching and breakup of the cavity tip. Visual observations showed predominantly entrained bubble sizes between 0.5 and 5 mm (Fig. 3-2B). Such millimetric size bubbles have a nearly constant bubble rise velocity (Appendix A). That is, the rise velocity $u_r \approx 0.25$ to 0. 3 m/s in freshwater and in seawater.

At larger speeds, the air cavity developed all around the perimeter and most air was entrained by elongation, stretching and breakup of the ventilated cavity. BONETTO and LAHEY (1993), CHANSON and CUMMINGS (1994b), CUMMINGS and CHANSON (1997a) and CHANSON and BRATTBERG (1998) discussed this mechanism. Visually most entrained air bubbles/packets tended to follow a somewhat helicoidal trajectory. In Model 1, the rotation direction fluctuated irregularly at low frequency (less than 0.5 Hz). The direction seemed related to the rotation sense of the free-surface vortex and DETSCH and SHARMA (1990) reported a similar effect.

Although the bulk of entrained bubbles did not penetrate deeply and never reached the bottom of the flume (e.g. Fig. 3-2C & 3-2D), fine bubbles with sizes less than 0.5 to 1 mm were consistently observed at deeper depths. Visual observations showed that some tiny bubbles could be trapped in large vortical structures for a relatively long time before being ejected to another eddy or toward the free-surface. Fine bubbles were consistently observed next to the bottom and, in some cases, bubbles trapped in turbulent eddies could remain next to the floor for over three minutes.

Fig. 3-2 - Photographs of air bubble entrainment at circular plunging jet

(A) Individual air bubble entrainment in Model 1 (d_o = 0.025 mm, Freshwater), x_1 = 0.100 m, V_1 = 2.05 m/s, Fr_1 = 4.3 - High speed photograph taken at night - Note the impingement perimeter (dark oval on top centre), the single-tip conductivity probe on the right and rising air bubbles - For scale, the vertical probe holder has a 3.3 mm diameter



(B) Model 2 (d_o = 0.0125 mm, Freshwater), x_1 = 0.1055 m, V_1 = 2.01 m/s, Fr_1 = 6.3



(C) Model 4 (d_o = 0.0125 mm, Seawater), x_1 = 0.050 m, V_1 = 2.46 m/s, Fr_1 = 7.2



(D) Model 5 (d_o = 0.0125 mm, Salty freshwater), x_1 = 0.0975 m, V_1 = 3.24 m/s, Fr_1 = 10.7



Discussion

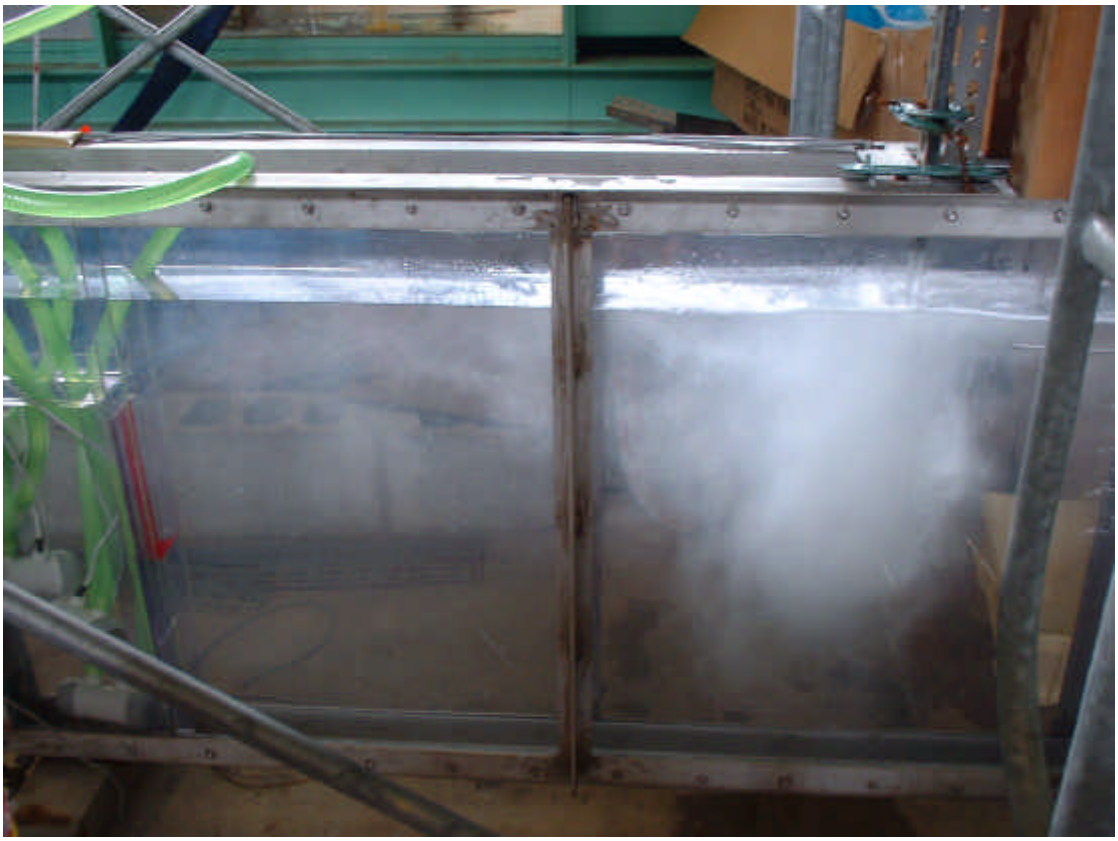
When identical experiments were conducted with different water solutions (i.e. freshwater, seawater, salty freshwater), the visual appearance of the bubbly flow region exhibited some differences. The following comments are subjective, they may vary between researchers, but they summarise the overall feeling of two senior researchers and three research students involved in the study.

In freshwater (Models 1, 2 & 3), the downward bubbly flow region was clearly defined and surrounded by rising bubbles. The flume waters appeared clear and transparent away from the plunging jet flow (e.g. Fig. 1-2C & 3-2B).

For identical inflow conditions, seawater experiments (Model 4) appeared to entrain more fine bubbles than freshwater plunging jets (Model 2), particularly for the largest inflow Froude numbers (i.e. $Fr_1 > 8$). Although the writers observed the entrainment of both millimetric and sub-millimetric bubbles, a large number of tiny bubbles (sizes less than 0.5 mm) were seen in the entire flume. These fine bubbles were strongly affected by large recirculation eddies and their rise velocity appeared very small. Figure 3-3 shows entrained bubbles few seconds after the start of the pumps. The grey nozzle and the downward bubbly flow region are seen on the right. On the left, the channel is transparent and a cloud of fine bubbles is seen propagating from the bubbly flow region toward the left end of the flume. When the pumps were stopped after a seawater experiment, fine bubbles would take up to few minutes to rise to the free-surface. The flume waters regained a clear, transparent appearance after about 2 to 5 minutes.

In salty freshwater (Model 5), visual observations suggested a lesser presence of fine bubbles than during seawater experiments, but certainly more than in freshwater experiments. Such a trend is reasonably consistent with chord time measurements, although the latter indicated a large majority of entrained millimetric bubbles for all water solutions (see paragraph 5.).

Fig. 3-3 - Air bubble entrainment at circular plunging jet with seawater : Model 4 (d_o = 0.025 mm, Seawater), x_1 = 0.050 m, V_1 = 3.13 m/s, Fr_1 = 9.1
Unsteady flow immediately after the pump start - Note the fine bubble clouds propagating horizontally beneath the free-surface, away from the impingement - Compare the air-water flow pattern with Fig. 1-2C



4. EXPERIMENTAL RESULTS. (2) DISTRIBUTIONS OF VOID FRACTIONS AND BUBBLE COUNT RATES

4.1 Introduction

The diffusion of air bubbles in a turbulent plunging jet flow can be approximated by an analytical solution of the diffusion equation (CHANSON 1995, 1997). For a circular plunging jet, the diffusion equation in cylindrical coordinates is :

$$\frac{\partial}{\partial x}(C * V) = \frac{1}{r} * \frac{\partial}{\partial r}\left(D_t * r * \frac{\partial C}{\partial r}\right) \quad (4\text{-}1)$$

where x is the longitudinal direction, r is the radial direction, C is the void fraction, V is the longitudinal velocity component in the x-direction and D_t is the air bubble turbulent diffusivity in the radial direction (Fig. 2-1). A solution of the air bubble diffusion equation is a series of Bessel functions :

$$C = \frac{Q_{air}}{Q_w} * \frac{1}{4 * D^{\#} * \frac{x - x_1}{r_1}} * \exp\left(- \frac{1}{4 * D^{\#}} * \frac{\left(\frac{r}{r_1}\right)^2 + 1}{\frac{x - x_1}{r_1}} \right) * I_o\left(\frac{1}{2 * D^{\#}} * \frac{\frac{r}{r_1}}{\frac{x - x_1}{r_1}} \right) \quad (4\text{-}2)$$

where Q_{air} is the strength of a circular source located at $\{x = x_1, r = r_1\}$, Q_w is the water discharge, V_1 is the jet impact velocity, x_1 is the jet impact coordinate, I_o is the modified Bessel function of the first kind of order zero ([7]) (Table 4-1). $D^{\#}$ is a dimensionless air bubble diffusivity defined as :

$$D^{\#} = \frac{D_t}{V_1 * r_1} \quad (4\text{-}3)$$

Equation (4-2) is a three-dimensional solution of the diffusion equation. It is valid in both developing bubbly region and fully-aerated flow region. The jet centreline (i.e. r = 0) becomes aerated for:

$$\frac{x - x_1}{r_1} > \frac{0.039}{D^{\#}} \quad \text{Fully-aerated jet flow region} \quad (4\text{-}4)$$

4.2 Void fraction distributions

Void fraction and bubble count rate measurements were conducted in the developing flow region : i.e., $(x - x_1)/r_1 < 5$. The full data set is presented in Appendix B. All experimental profiles traversed the full width of the developing flow region and are shown on the figures to emphasise symmetry (or the absence of symmetry in few specific cases). Consequently an apparently negative radius appears on the Figures. Figures 4-1A and 4-1B present freshwater experimental data for impact Froude numbers Fr_1 = 8.8 and 9.2 respectively, at three vertical locations $(x-x_1)/r_1$ where x is the longitudinal coordinate, x_1 is the jet length and r_1 is the jet radius at impact (Fig. 2-1). Figures 4-1C and 4-1D show data obtained in seawater (Model 4) and in salty freshwater (Model 5) respectively for Fr_1 = 9. The inflow conditions (Fr_1 = 9, x_1/d_o = 4) are identical in Figures 4-1B, 4-1C & 4-1D.

[7] $I_o(u) = 1 + \frac{u^2}{2^2} + \frac{u^4}{2^2 * 4^2} + \frac{u^6}{2^2 * 4^2 * 6^2} + \ldots$

Table 4-1 - Values of the modified Bessel function of the first kind of order zero

u	I_o	u	I_o	u	I_o
(1)	(2)	(1)	(2)	(1)	(2)
0	1	2.0	2.280	4.0	11.30
0.1	1.003	2.1	2.446	4.1	12.32
0.2	1.010	2.2	2.629	4.2	13.44
0.3	1.023	2.3	2.830	4.3	14.67
0.4	1.040	2.4	3.049	4.4	16.01
0.5	1.063	2.5	3.290	4.5	17.48
0.6	1.092	2.6	3.553	4.6	19.09
0.7	1.126	2.7	3.842	4.7	20.86
0.8	1.167	2.8	4.157	4.8	22.79
0.8	1.213	2.9	4.503	4.9	24.91
1	1.266	3.0	4.881	5.0	27.24
1.1	1.326	3.1	5.294	5.1	29.79
1.2	1.394	3.2	5.747	5.2	32.58
1.3	1.469	3.3	6.243	5.3	35.65
1.4	1.553	3.4	6.785	5.4	39.01
1.5	1.647	3.5	7.378	5.5	42.69
1.6	1.750	3.6	8.028	5.6	46.74
1.7	1.864	3.7	8.739	5.7	51.17
1.8	1.990	3.8	9.517	5.8	56.04
1.9	2.128	3.9	10.37	5.9	61.38

Notes : Reference: SPIEGEL (1974); For low values of u, I_o can be approximated by : $I_o(u) = 1 + \frac{u^2}{2^2} + \frac{u^4}{2^2 * 4^2}$; For large values of u, I_o can be approximated by : $I_o(u) = \exp(u)/\sqrt{2*\pi*u}$.

In the developing flow region, the distributions of void fraction exhibited smooth, derivative profiles (Fig. 4-1). In each experiment, the data illustrated consistently the advective diffusion of entrained air associated with a quasi-exponential decay of maximum air content with longitudinal distance from impingement and a broadening of the air diffusion layer. For all experiments and jet geometry, the data were best fitted by :

$$C = \frac{Q_{air}}{Q_w} * \frac{1}{4 * D^{\#} * \frac{x - x_1}{Y_{Cmax}}} * \exp\left(- \frac{1}{4 * D^{\#}} * \frac{\left(\frac{r}{Y_{Cmax}}\right)^2 + 1}{\frac{x - x_1}{Y_{Cmax}}} \right) * I_o\left(\frac{1}{2 * D^{\#}} * \frac{\frac{r}{Y_{Cmax}}}{\frac{x - x_1}{Y_{Cmax}}} \right) \qquad (4\text{-}5)$$

where $Y_{Cmax} = r(C=C_{max})$ was measured (Fig. 4-2D). Equation (4-5) is shown in Figure 4-1. The values of $D^{\#}$ and Q_{air}/Q_w were determined from the best fit of the data and are given in Table 4-2 (columns 9 & 10).

Equation (4-5) differs slightly from the analytical solution of the advective diffusion equation (i.e. Eq. (4-2)). For each experiment, the ratio Y_{Cmax}/r_1 was found consistently to be equal to or greater than unity, with increasing value with increasing distance $(x-x_1)/r_1$ from impingement point. Experimental values of Y_{Cmax}/r_1 and corresponding maximum void fraction C_{max} are presented in Table 4-2 (columns 5 & 6). Figures 4-2A and 4-2C show respectively observations of C_{max} and Y_{Cmax} for identical inflow conditions (i.e. $x_1/d_o = 4$, $Fr_1 = 9$) in freshwater (Models 1, 2 and 3), seawater (Model 4) and salty freshwater (Model 5). Figure 4-2A illustrates nearly identical results between Models 1 and 2 in freshwater, and a marked reduction in maximum

void fraction C_{max} for the smallest plunging jet (Model 3). Results in seawater (Model 4) and saltwater (Model 5) show smaller maximum void fractions than in freshwater for identical jet diameter (Model 2), although the locations of maximum void fractions appear unaffected by the type of water solutions (Fig. 4-2C).

4.3 Bubble count rate distributions

Distributions of bubble count rates were also recorded in the developing flow region (Fig. 4-1, Appendix B). The results highlighted maximum bubble frequency in the developing shear layers. Detailed observations of maximum bubble count rates F_{max} and their location Y_{Fmax} are presented in Table 4-2 (columns 7 & 8). Figure 4-2 shows experimental observations obtained for identical inflow conditions (i.e. $x_1/d_o = 4$, $Fr_1 = 9$) in freshwater (Models 1, 2 and 3), seawater (Model 4) and salty freshwater (Model 5).

Consistently, the maximum bubble count rate occurred in the inner shear region : i.e., at a distance Y_{Fmax} from the jet centreline that was smaller than the location Y_{Cmax} where the void fraction was maximum (Fig. 4-2D). Such a result ($0 < Y_{Fmax} < Y_{Cmax}$) was previously observed in circular plunging jets (MANASSEH and CHANSON 2001) and in two-dimensional jets (BRATTBERG and CHANSON 1998). BRATTBERG and CHANSON hypothesised that this was caused by "*the non-coincidence between the air bubble diffusion layer and the momentum shear layer*". During the present study, air-water velocities were not recorded, but their comments may still be appropriate. Figure 4-3 presents typical relationships between dimensionless bubble count rate and void fraction. Although this relationship was found to be unique in self-aerated chute flows and in air-water jets discharging into air (e.g. BRATTBERG et al. 1998, TOOMBES 2002), the relationship void fraction/bubble count rate exhibits some hysteresis in the developing region of plunging jet flows. For a given void fraction, greater bubble count rate was observed in the inner developing flow region. Note, in Figure 4-3, that there is some difference between the left and right shear layers at a given cross-section (see also Fig. 4-1).

Remarks

For any bubble size shape, bubble size distribution and chord length distribution, the mean chord length size (i.e. number mean size) ch_{mean} is related to the air content, velocity and bubble frequency by:

$$ch_{mean} = \frac{C * V}{F} \quad (4\text{-}6)$$

where V is the air-water velocity. Although local velocities were not measured, the characteristic velocity in the developing shear region was about or greater than $V_1/2$ for which experimental data implied mean bubble sizes of about ch_{mean} ~ 3.4 and 2.3 mm in Models 1 and 2 respectively. Such estimates are consistent with measured bubble chord times (see discussion in paragraph 5.).

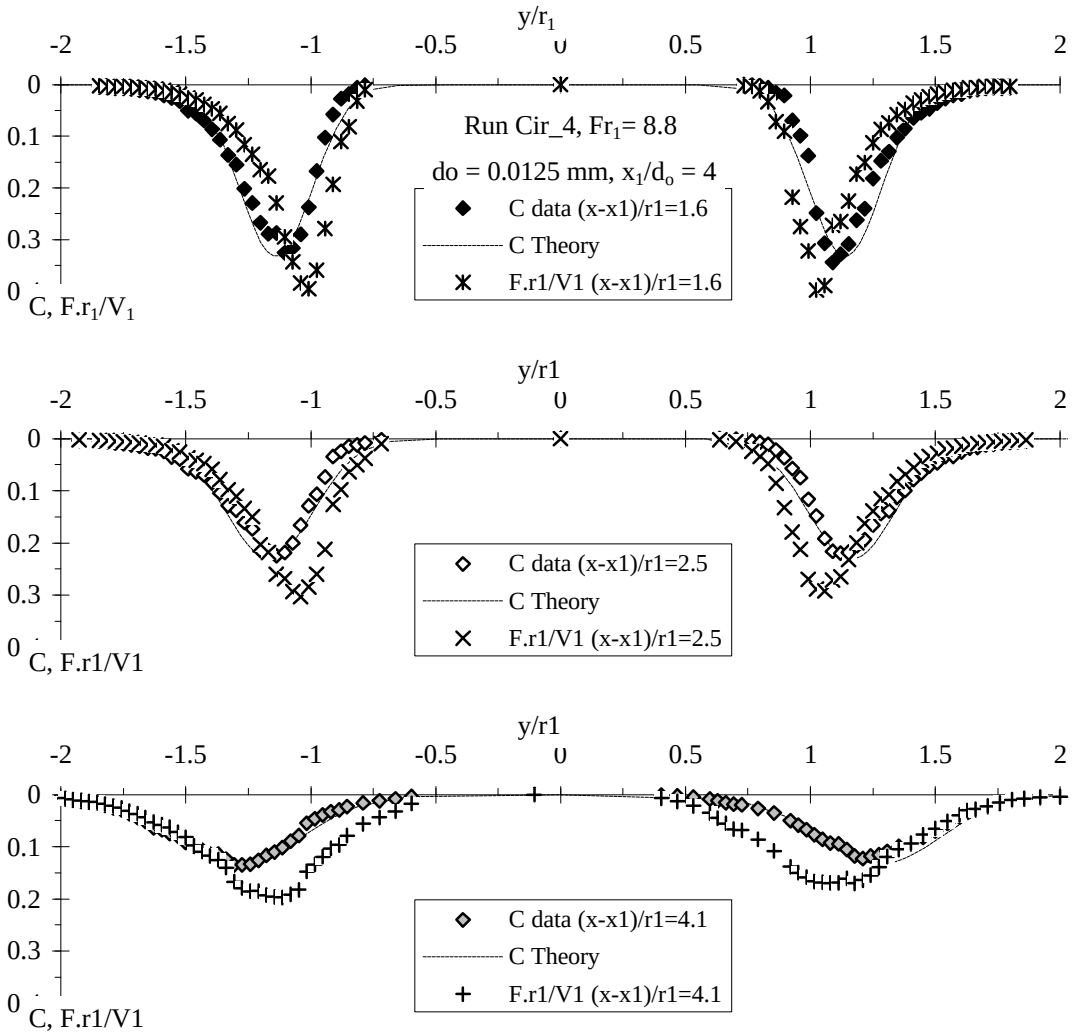
Table 4-2 - Characteristics air-water flow measurements in vertical circular plunging jets

Run	V_1	Fr_1	$\frac{x-x_1}{r_1}$	$\frac{Y_{Cmax}}{r_1}$	C_{max}	$\frac{Y_{Fmax}}{r_1}$	$\frac{F_{max}*r_1}{V_1}$	$\frac{Q_{air}}{Q_w}$	$D^{\#}$	Remarks
	m/s							([1])	([1])	
(1)	(2)	(3)	(4)	(5)	(6)	(7)	(8)	(9)	(10)	(11)
Model 1										Freshwater.
BM35_1	3.5	7.22	1.67	1.08	0.23	1.07	0.32	0.108	3.4E-3	
			2.51	1.18	0.16	1.12	0.23	0.100	4.0E-3	
			4.18	1.18	0.08	1.19	0.16	0.085	6.3E-3	
BM4_2	4.1	8.41	1.65	1.11	0.36	1.05	0.38	0.178	5.2E-3	
			2.48	1.20	0.23	1.09	0.29	0.174	5.0E-3	
			4.13	1.25	0.19	1.14	0.23	0.180	6.0E-3	
BM44_2	4.4	9.00	1.64	1.11	0.39	1.06	0.42	0.193	5.0E-3	
			2.46	1.17	0.27	1.08	0.34	0.193	5.0E-3	
			4.11	1.27	0.19	1.17	0.26	0.180	5.5E-3	
Model 2										Freshwater
Cir_2	2.42	7.07	1.67	*1.22*	*0.21*	*1.15*	*0.32*	0.160	7.0E-3	
			2.51	*1.24*	*0.11*	*1.19*	*0.18*	0.105	6.5E-3	
			4.19	1.38	0.06	1.32	0.11	0.060	6.0E-3	
Cir_4	3.04	8.81	1.65	1.09	0.33	1.01	0.40	0.240	6.5E-3	
			2.47	1.12	0.22	1.04	0.30	0.200	6.0E-3	
			4.11	1.24	0.13	1.14	0.18	0.160	7.2E-3	
Cir_5	3.18	9.20	1.64	1.10	0.36	1.02	0.40	0.280	6.5E-3	
			2.46	1.14	0.22	1.04	0.32	0.200	7.0E-3	
			4.10	1.25	0.15	1.10	0.24	0.190	7.0E-3	
Cir_6	3.46	9.98	1.63	1.12	**0.53**	1.03	**0.45**	0.410	7.0E-3	
			2.45	1.05	**0.42**	1.05	0.25	0.390	7.0E-3	
			4.09	1.29	**0.31**	1.10	0.20	0.400	9.0E-3	
Model 4										Seawater
Sea_2	2.46	7.19	1.67	*1.13*	*0.15*	*1.08*	*0.21*	0.110	6.0E-3	
			2.51	*1.05*	*0.07*	*1.25*	*0.11*	*0.090*	*6.0E-3*	
			4.18	1.24	0.06	1.19	0.10	0.065	6.5E-3	
Sea_4	2.87	8.34	1.65	1.13	0.22	1.08	0.28	0.159	6.0E-3	
			4.13	1.31	0.10	1.16	0.13	0.105	5.8E-3	
Sea_5	3.13	9.07	1.64	1.17	0.24	1.08	0.32	0.193	6.3E-3	
			2.46	1.17	0.16	1.09	0.19	0.150	6.3E-3	
			4.11	1.23	0.11	1.18	0.17	0.130	6.3E-3	
Sea_6	3.36	9.70	1.64	1.18	0.25	1.08	0.31	0.193	6.5E-3	
			2.46	1.13	0.18	1.06	0.30	0.172	6.3E-3	
			4.09	1.26	0.11	1.21	0.17	0.170	6.3E-3	
Model 5										Salty freshwater
Salt_5	3.12	9.04	1.64	1.14	0.32	1.07	0.40	0.240	6.1E-3	
			2.46	1.17	0.16	1.09	0.25	0.140	5.5E-3	
			4.11	1.22	0.12	1.09	0.20	0.140	5.0E-3	
Model 3										Freshwater
Run-1	1.79	7.09	1.69	1.07	0.04	1.04	0.05	0.030	8.0E-3	
			2.51	1.10	0.03	1.04	0.05	0.030	8.0E-3	
			4.20	1.13	0.02	0.95	0.04	0.031	9.0E-3	
Run-2	2.16	8.46	1.66	1.15	0.11	1.15	0.11	0.070	4.5E-3	
			2.48	1.12	0.06	1.09	0.09	0.045	4.0E-3	
			4.14	1.18	0.03	1.06	0.05	0.033	5.0E-3	
Run-3	2.30	9.00	1.65	1.17	0.12	1.11	0.14	0.075	4.7E-3	
			2.47	1.17	0.08	1.08	0.10	0.060	4.7E-3	
			4.12	1.17	0.04	0.99	0.07	0.047	5.5E-3	
Run-4	2.49	9.74	1.65	1.43	0.23	1.32	0.17	0.200	9.0E-3	
			2.46	1.39	0.19	1.29	0.15	0.190	8.0E-3	
			4.10	1.36	0.10	1.18	0.10	0.155	1.1E-2	

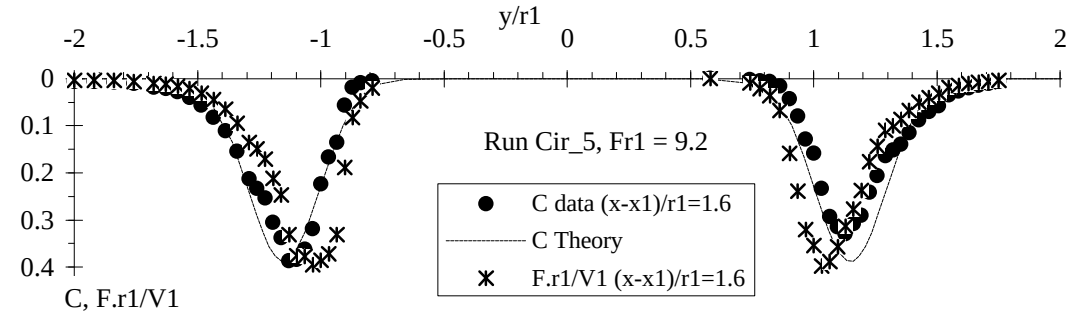
Notes : ([1]) : best fit between Equation (4-5) and data; **Bold data** : very-suspicious experimental data; *Italic data* : doubtful data.

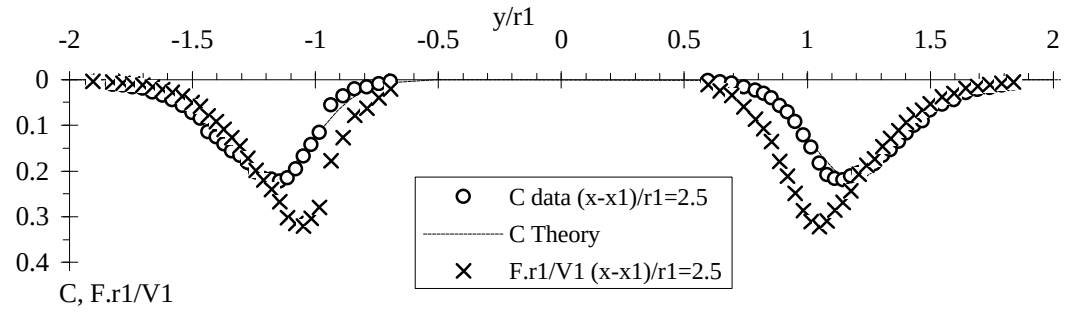
Fig. 4-1 - Dimensionless distributions of void fraction C and bubble count rate F^*r_1/V_1 in vertical circular jets
Comparison between experimental data and Equation (4-5)

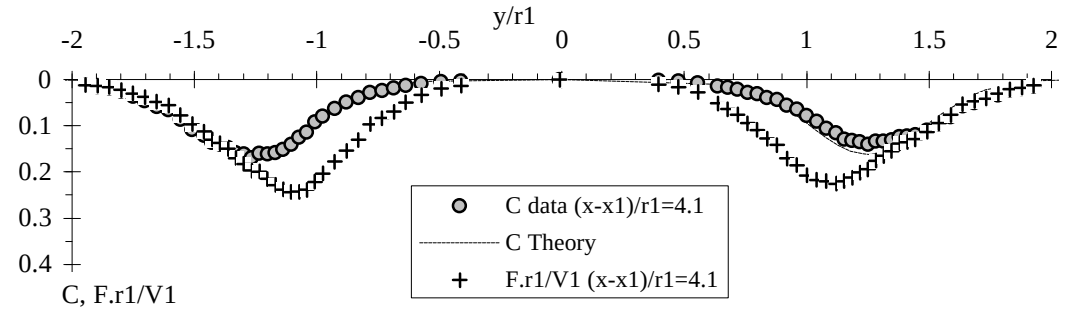
(A) Model 2 (d_o = 0.0125 m, Freshwater), x_1 = 0.05 m V_1 = 3.0 m/s, Fr_1 = 8.8 (Run Cir_4)



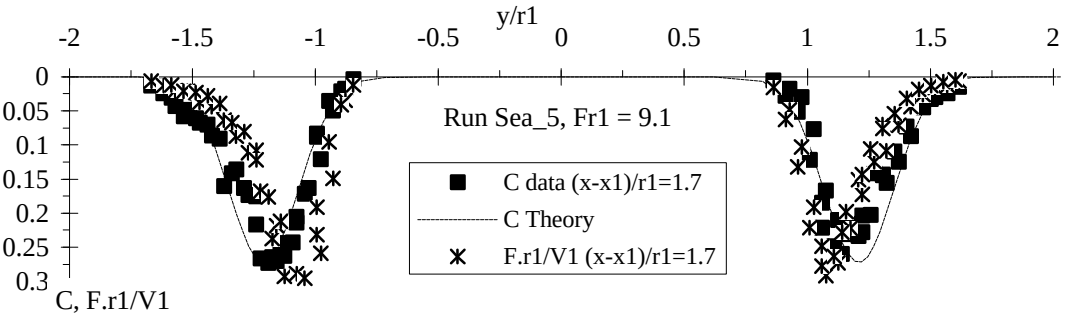
(B) Model 2 (d_o = 0.0125 m, Freshwater), x_1 = 0.05 m V_1 = 3.18 m/s, Fr_1 = 9.2 (Run Cir_5)

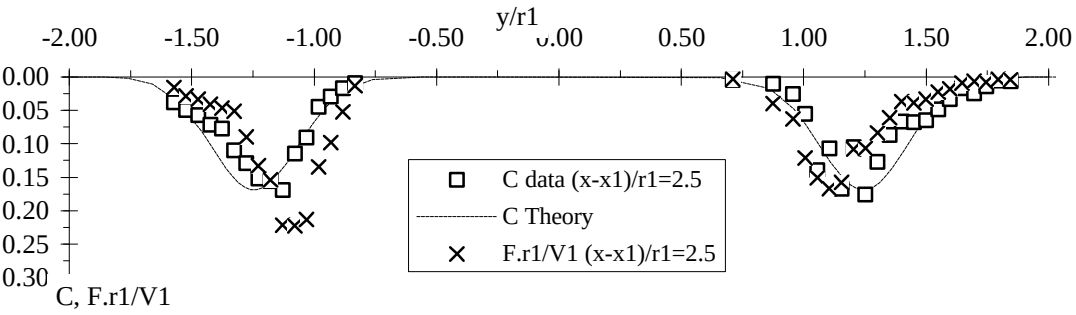


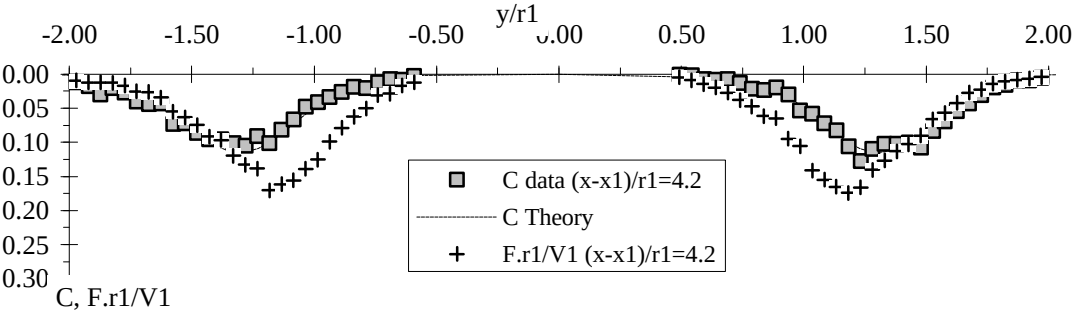




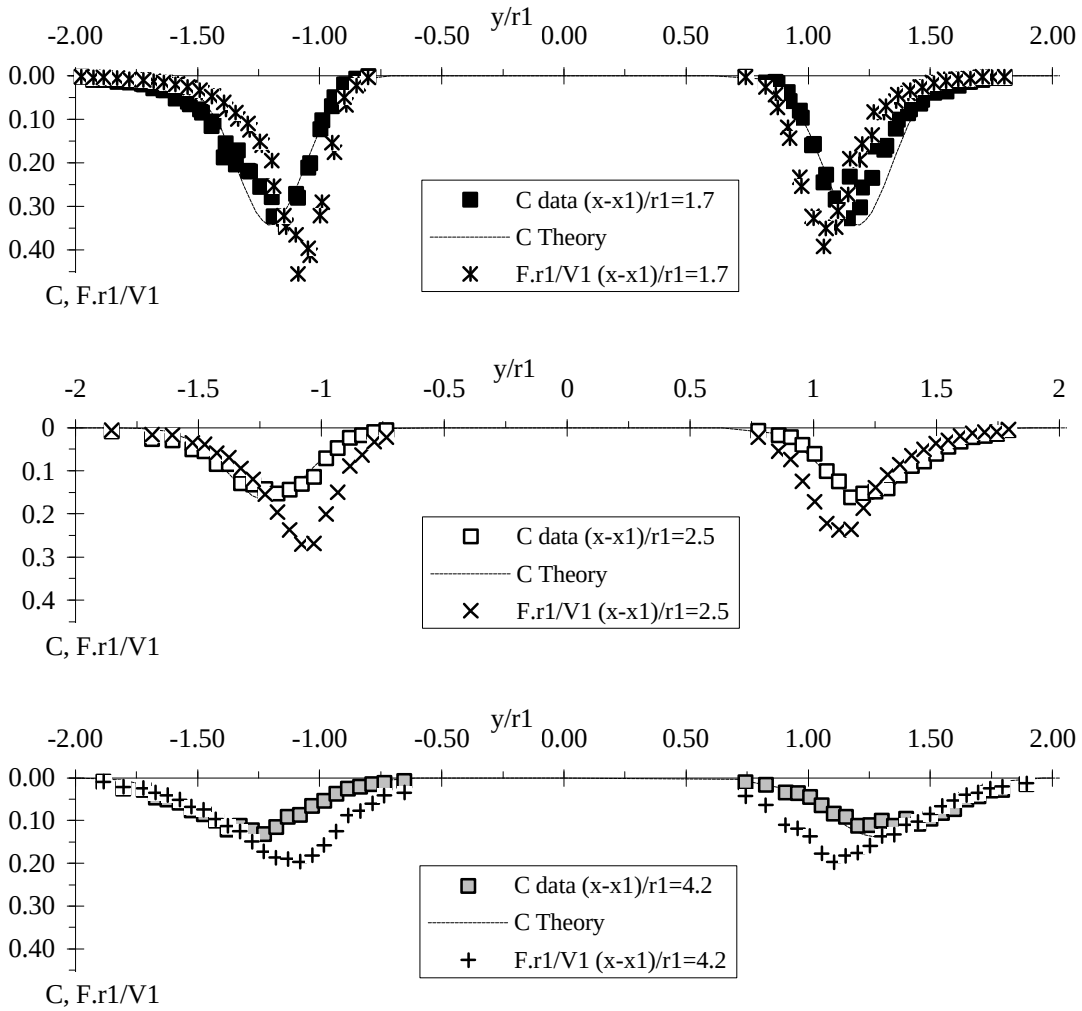
(C) Model 4 (d_o = 0.0125 m, Seawater), x_1 = 0.05 m V_1 = 3.13 m/s, Fr_1 = 9.1 (Run Sea_5)







(D) Model 5 (d_o = 0.0125 m, Salty freshwater), x_1 = 0.05 m V_1 = 3.12 m/s, Fr_1 = 9.0 (Run Sea_5)



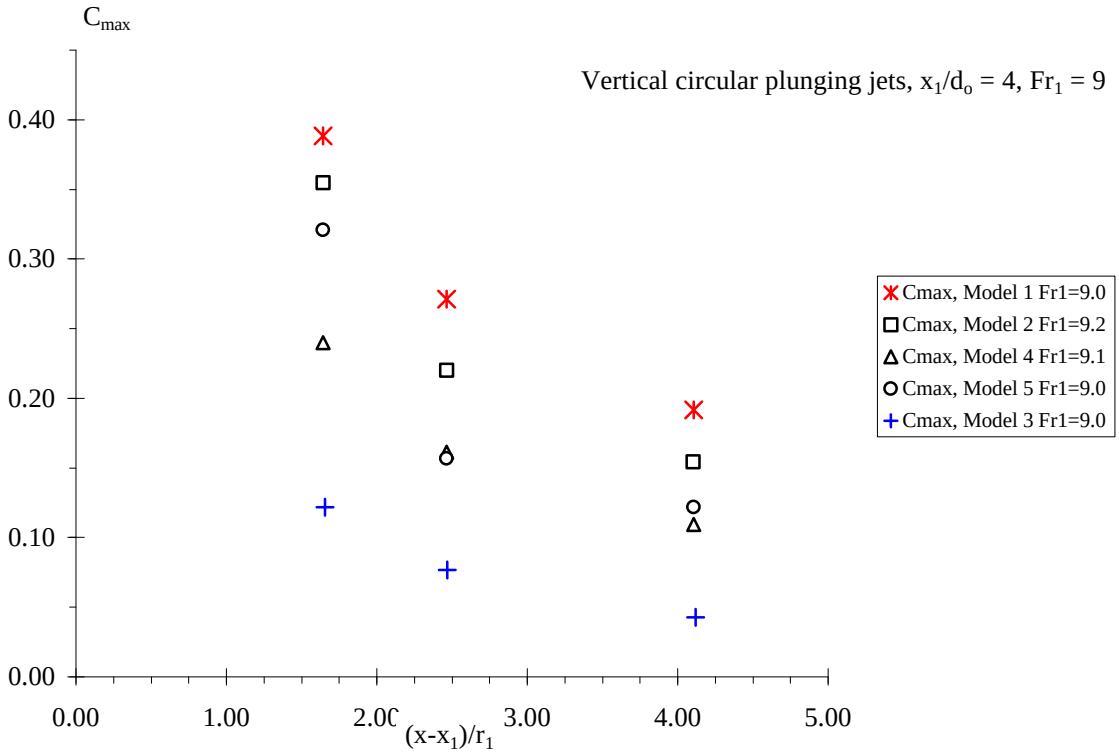
For any bubble size distribution and chord length distribution, the specific air-water interface area derives from the mass conservation for air :

$$a = \frac{4 * F}{V} \qquad (4\text{-}7)$$

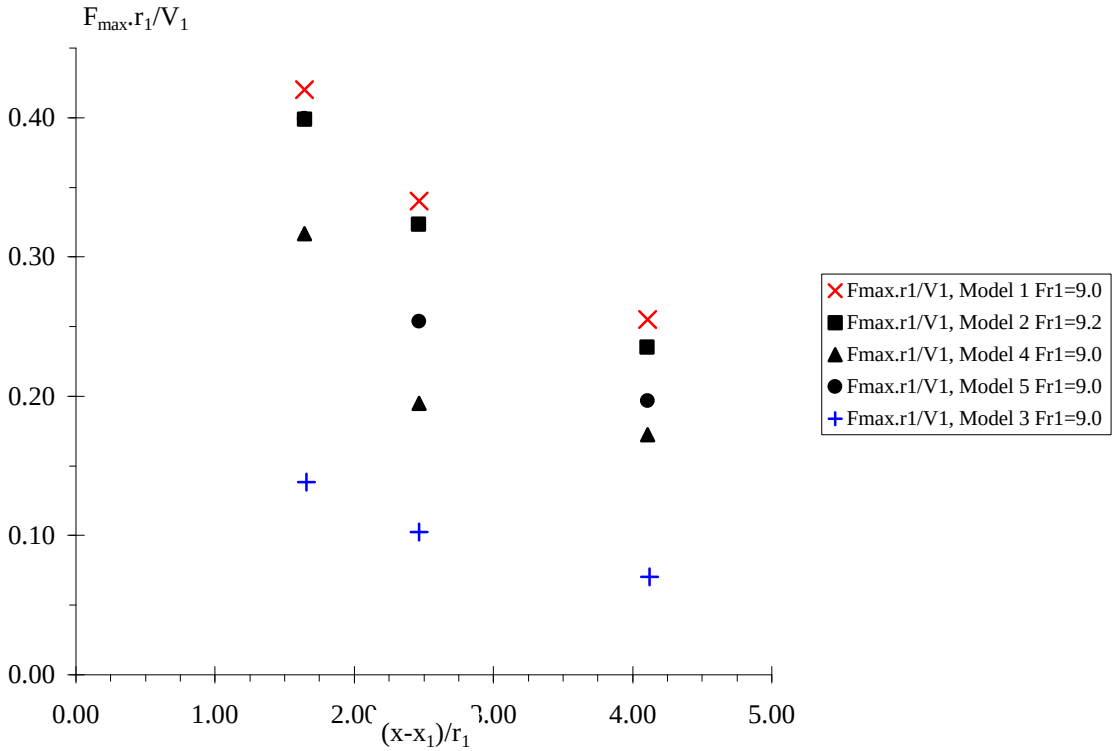
where a is the air-water surface area per unit volume of air and water. The derivation of (4-7) is simple for spherical particles. It may be extended to ellipsoidal particles following the method of CLARK and TURTON (1988) (also MOURSALIE et al. 1995). When the flow structure is more complex, the result (Eq. (4-7)) is not exactly the true specific interface area. Then, a becomes simply proportional to the number of air-water interfaces per unit length of air-water mixture : that is, $a \propto 2*F/V$. While V was not measured in the present study, an order of magnitude of the air-water velocity in the developing flow is about $V_1/2$. Measured bubble count rates imply maximum specific interface area between 25 and 130 m^{-1} in Models 1 and 2 depending upon the inflow Froude number and distance below impingement.

Fig. 4-2 - Experimental observations of maximum void fractions and dimensionless bubble count rates in vertical circular jet flows for Fr_1 = 9 and x_1/d_o = 4 in freshwater (Models 1, 2 & 3), seawater (Model 4) and salty freshwater (Model 5)

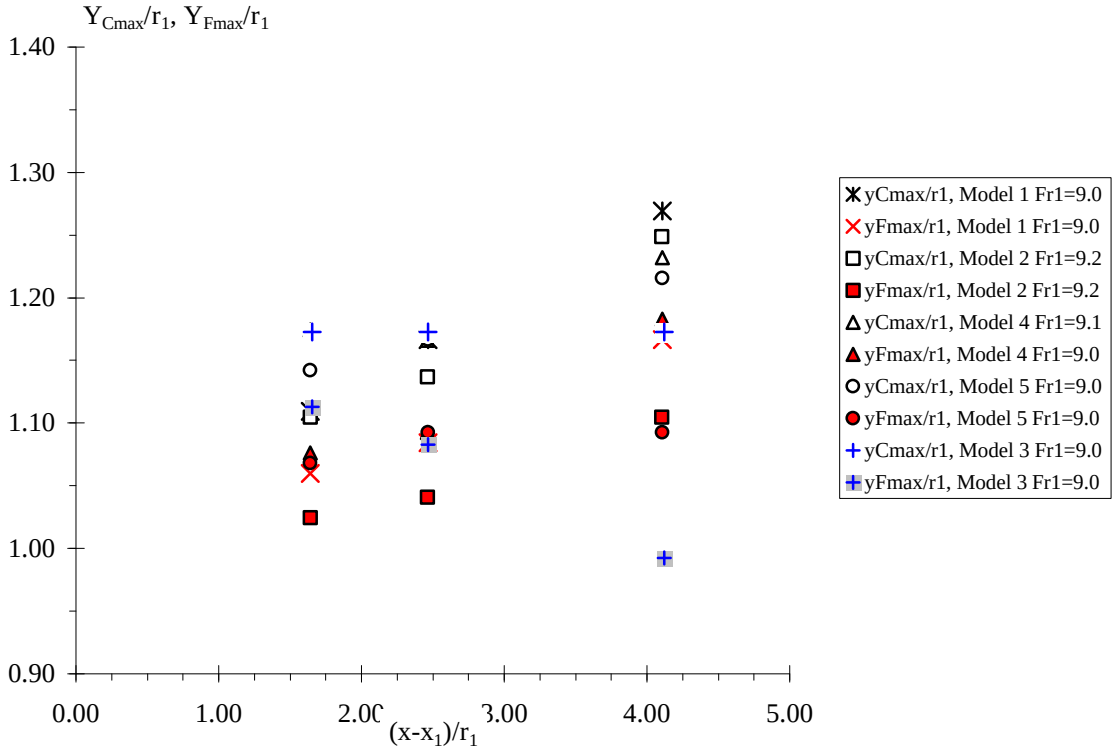
(A) Maximum void fractions C_{max}



(B) Maximum dimensionless bubble count rate $F_{max}*r_1/V_1$



(C) Dimensionless locations of maximum void fractions and maximum bubble count rates



(D) Definition sketch

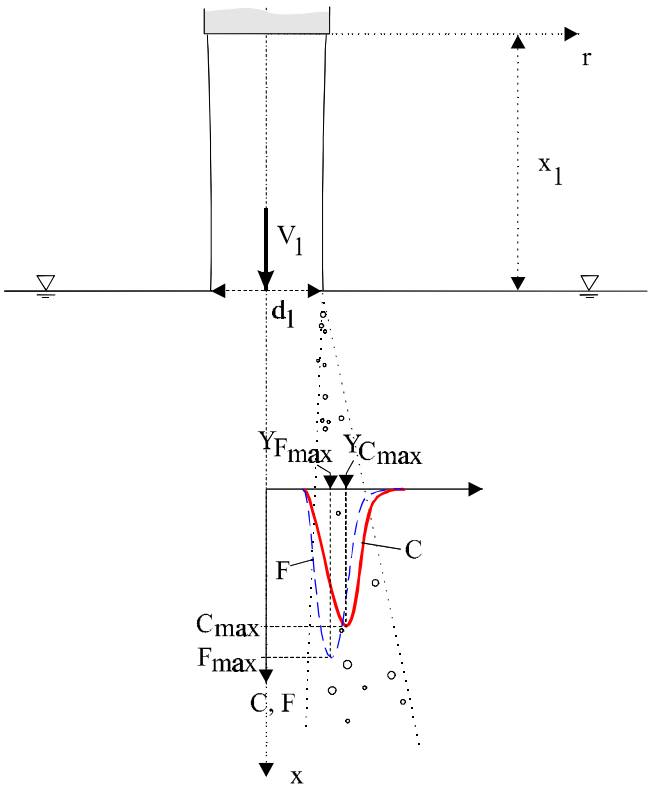
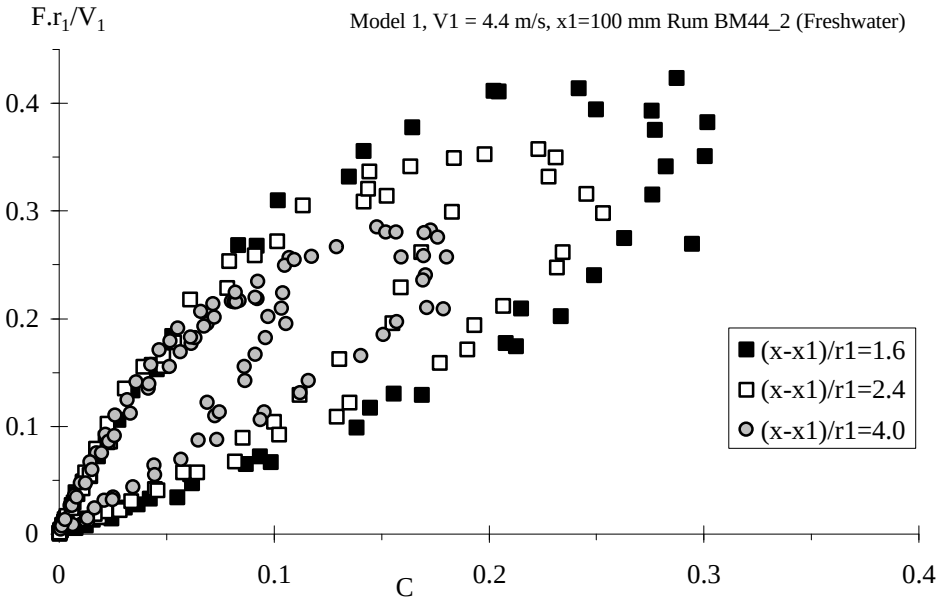


Fig. 4-3 - Relationship between void fraction and dimensionless bubble count rate at a given cross-section in vertical circular jet flows

Model 1 (d_o = 0.025 m, Freshwater), x_1 = 0.1 m V_1 = 4.4 m/s, Fr_1 = 9.0 (Run BM44_2)



4.4 Discussion

4.4.1 Scale effects in freshwater plunging jets

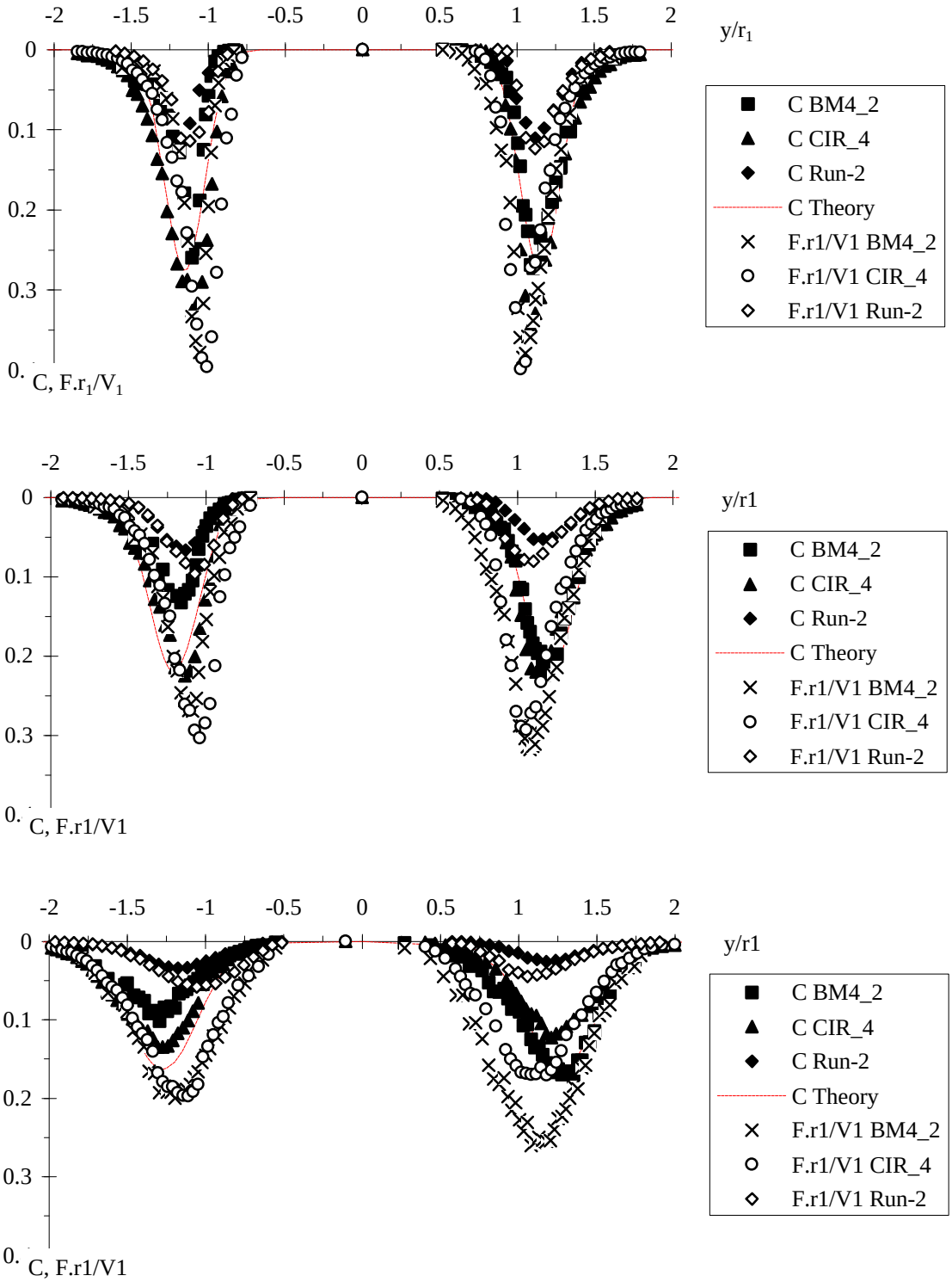
In freshwater plunging jets, experimental data observed in the two largest models (i.e. Models 1 & 2) are basically identical at each cross-section for Fr_1 = 8.4 and 9.1 (e.g. Fig. 4-4A). Figure 4-4A shows a comparison for one inflow Froude number. Differences between Models 1 and 2 were noted however for the lowest Froude number Fr_1 = 7 (Fig. 4-4B). Model 2 data showed a faster decay in void fraction and bubble count rate with increasing distance $(x-x_1)/r_1$ than observed in the larger Model 1 (Fig 4-4B, $(x-x_1)/r_1$ = 4). It is believed that, in the small-size Model 2 and for Fr_1 = 7, the detrainment rate was greater because the bubble rise velocity could not be scaled properly with a Froude similitude. The rise velocity was found to be nearly identical in all Models, and the velocity ratio V_1/u_r decreased with decreasing model size. The data (Fr_1 = 7) showed also some dissymmetry which might be attributed to a feedback mechanism between the probe and developing vortices. It is hypothesised that the probe support interfered with the developing shear region, preventing the development of helicoidal vortical structures. In turn air entrapment was affected and found to be lesser on one side or another.

For all investigated flow conditions (Table 2-1), significantly less air was entrained in Model 3 in comparison with Models 1 and 2. This is clearly seen in Figure 4-4 in terms of both void fraction and bubble count rate. It is believed that, in Model 3, air entrainment was affected by scale effects.

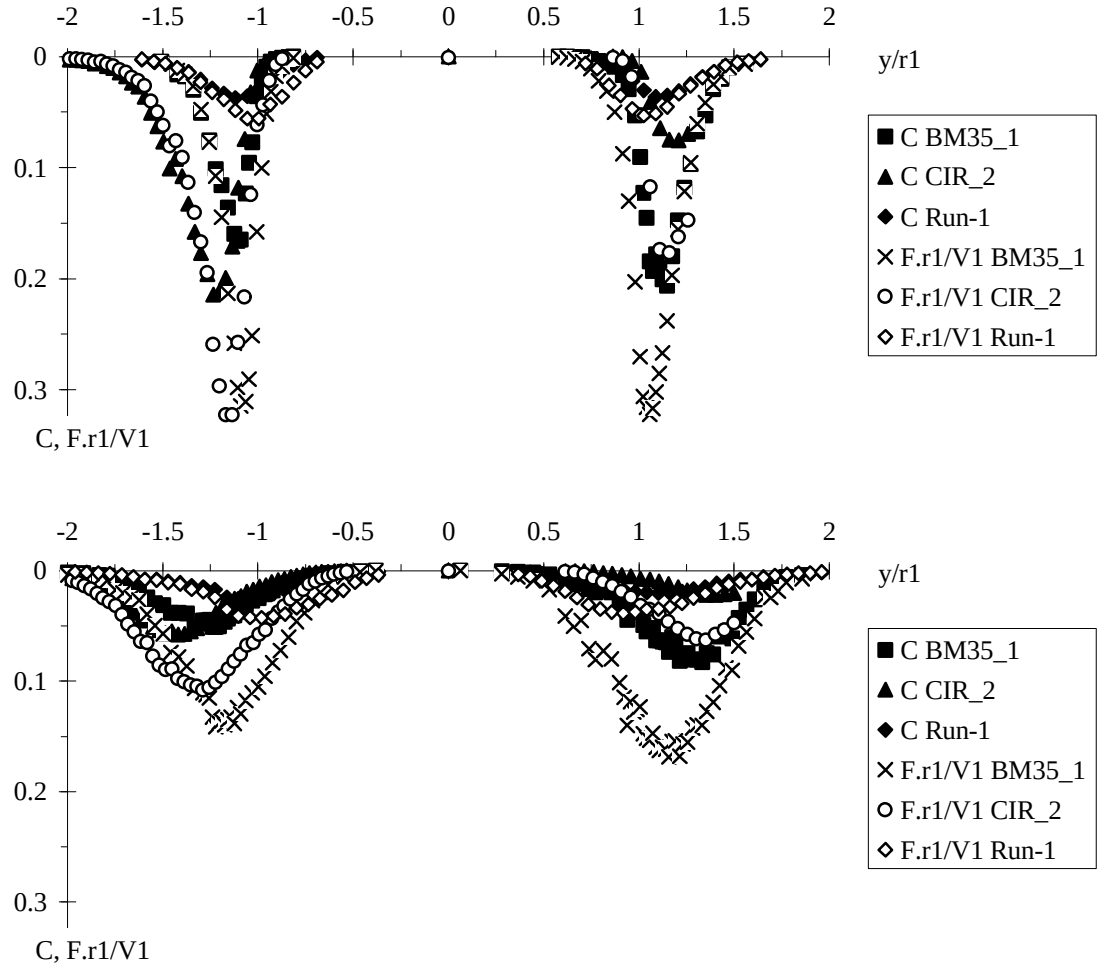
In summary, the present series of freshwater experiments showed air entrainment scale effects in Model 3 (i.e. $We_1 = \rho_w * V_1^2 * d_1/\sigma$ < 1E+3) and some detrainment scale effects in Model 2 for Fr_1 = 7 (i.e. V_1/u_r < 10).

Fig. 4-4 - Comparison of air-water flow properties in plunging jet flows of three geometric scales (Models 1, 2 and 3)

(A) Distributions of void fraction C and dimensionless bubble count rate F^*r_1/V_1 for identical inflow conditions (x_1/d_o = 4.0, Fr_1 = 8.4, Freshwater) : Model 1 (d_o = 0.025 m, run BM4_2), Model 2 (d_o = 0.0125 m, run Cir_4), Model 3 (d_o = 0.0068 m, run Run-2) - Comparison between experimental data and Equation (4-5) (for Model 1)



(B) Distributions of void fraction C and dimensionless bubble count rate F^*r_1/V_1 for identical inflow conditions (x_1/d_o = 4.0, Fr_1 = 7.1, Freshwater) : Model 1 (d_o = 0.025 m, run BM4_2), Model 2 (d_o = 0.0125 m, run Cir_4), Model 3 (d_o = 0.0068 m, run Run-2)



4.4.2 Comparative study of air entrainment in freshwater and seawater

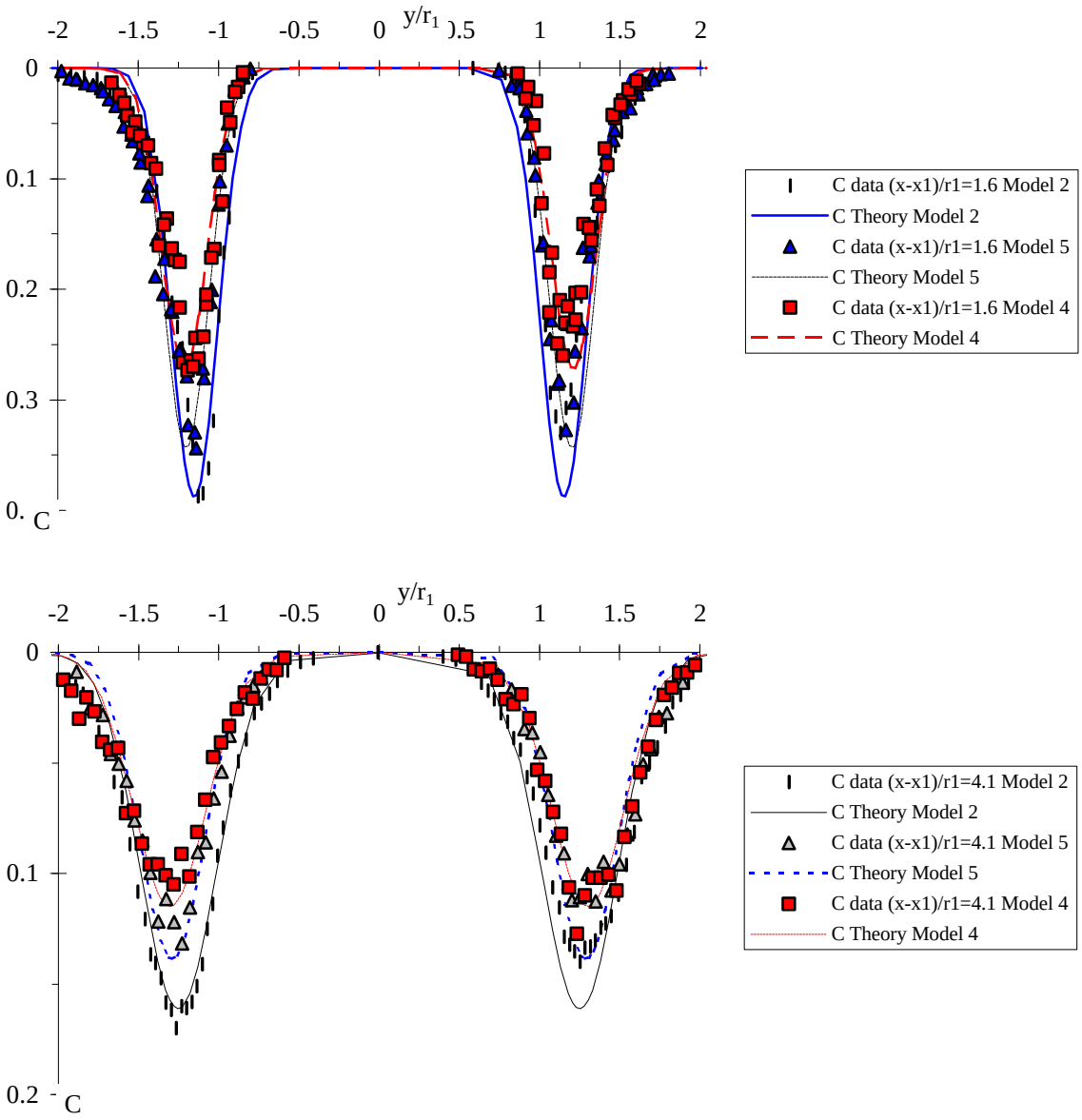
Experiments with identical inflow conditions were repeated with different water solutions : i.e., freshwater, seawater and salty freshwater (Table 2-1). Figure 4-5 presents a comparison for one inflow Froude number Fr_1 = 9 at two cross-sections $(x-x_1)/r_1$ = 1.6 & 4. Each data set is compared with the corresponding theoretical curve (i.e. Eq. (4-5)).

All the experiments showed consistently that, for identical inflow conditions (i.e. given x_1/d_o and Fr_1), greater void factions were observed in freshwater than in seawater and saltwater. The smallest void fractions were recorded in seawater and intermediate void fractions were seen in salty freshwater. The trend is illustrated in Figure 4-5A at $(x-x_1)/r_1$ = 1.6 & 4. Freshwater, seawater and saltwater data are shown respectively with diamond, square and triangle symbols. Freshwater data exhibit the largest void fractions, hence largest quantity of entrained air. The smallest void fractions are the seawater data. The trend is consistent with maximum void fraction data shown in Figure 4-2A. It is hypothesised that surfactants and bio-chemicals harden the induction trumpet (sketched in Fig. 1-3) and diminish air entrapment at impingement in seawater. Chord time results (paragraph 5.) suggest that lesser large-size bubbles were entrained in seawater compared to freshwater.

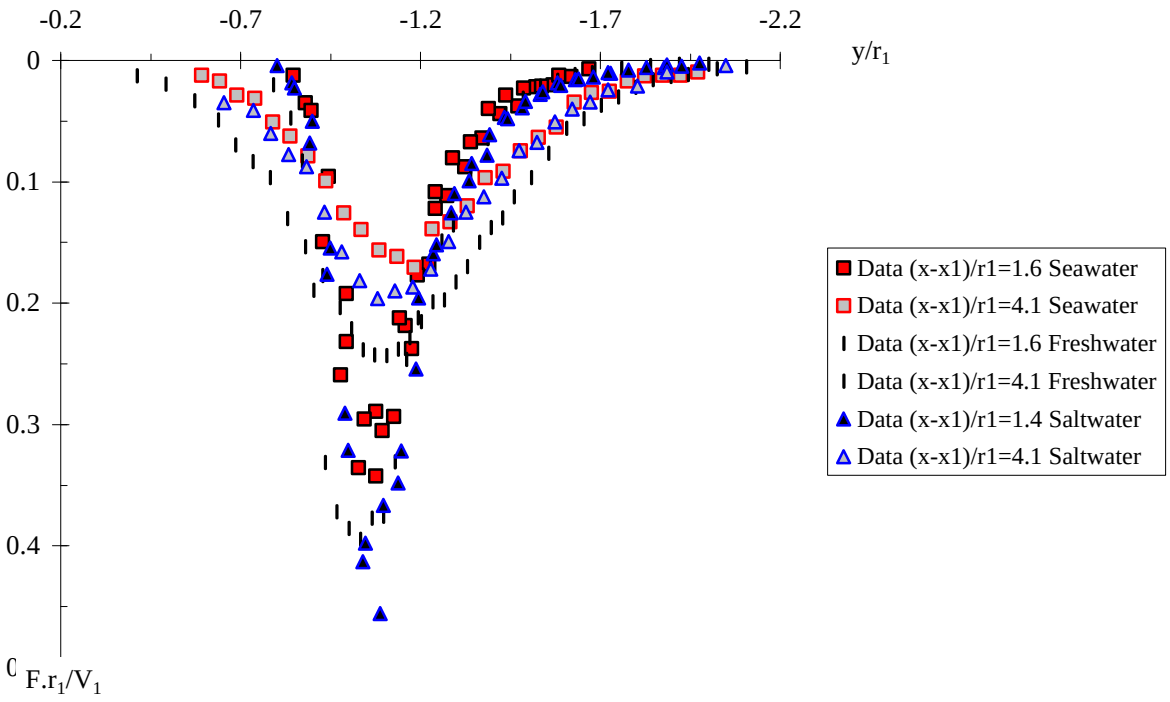
Bubble count rate data in freshwater are consistently greater than in seawater (Fig. 4-5B). Saltwater results show an intermediate trend between freshwater and seawater results.

Fig. 4-5 - Comparison of air-water flow properties in plunging jet flows for different water solutions (Models 2, 4 and 5) for Fr_1 = 9, d_o = 0.025 m and x_1/d_o = 4

(A) Distributions of void fraction C for identical inflow conditions : Model 2 (Freshwater, run Cir_5), Model 4 (Seawater, run Sea_5), Model 5 (Salty freshwater, run Salt_5) - Comparison between experimental data and Equation (4-5)



(B) Distributions of dimensionless bubble count rate F^*r_1/V_1 for identical inflow conditions : Model 2 (Freshwater, run Cir_5), Model 4 (Seawater, run Sea_5), Model 5 (Salty freshwater, run Salt_5)



5. EXPERIMENTAL RESULTS. (3) DISTRIBUTIONS OF BUBBLE CHORD TIMES

5.1 Definition

The bubble chord time is defined as the time spent by a bubble on the probe sensor. Chord time data were calculated from the raw signal scanned at 25 kHz for 2.6 seconds at 8 locations per cross-section. The results are presented in terms of pseudo-bubble chord length ch_{ab} defined as :

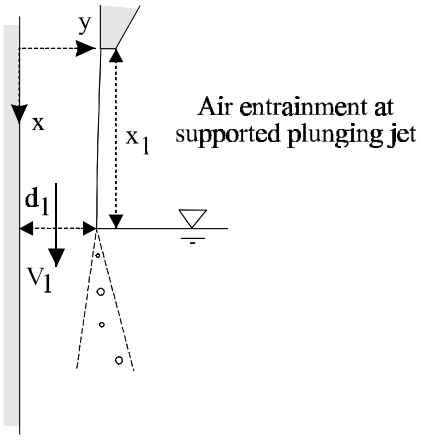
$$ch_{ab} = V_1 * t_{ch} \quad (5\text{-}1)$$

where t_{ch} is the bubble chord time and V_1 is the jet impingement velocity.

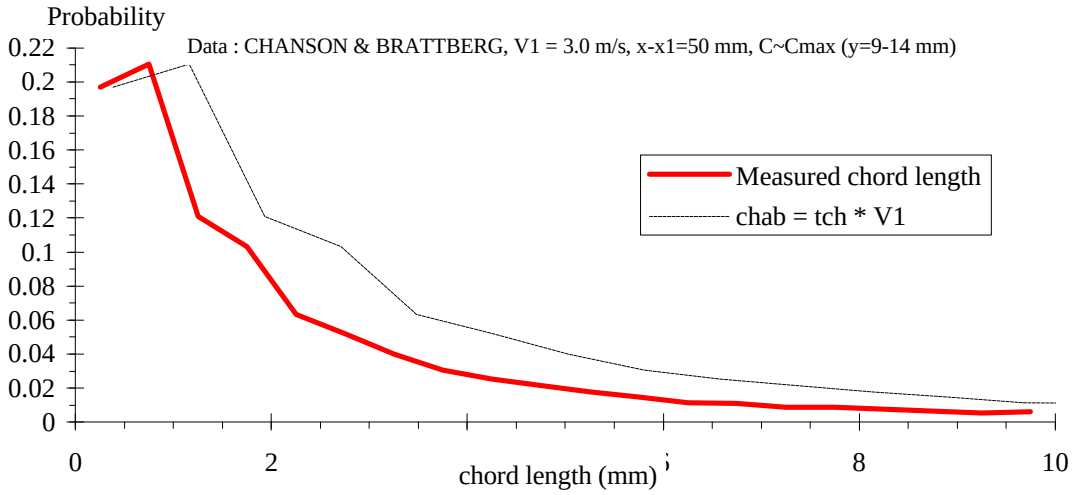
The pseudo bubble chord length ch_{ab} is not equal to the bubble chord length because the local air-water velocity V is smaller than the impingement velocity V_1. The experiments of CUMMINGS and CHANSON (1997b) and BRATTBERG and CHANSON (1998) in the developing flow region of two-dimensional plunging jets showed however that most entrained bubbles were advected in high-velocity shear region where $V_1/2 < V < V_1$. The writers re-analysed chord size data of CHANSON and BRATTBERG (1996) and CUMMINGS and CHANSON (1997b). (The latter data set was reported in CHANSON (1995) and CUMMINGS (1996).) Figure 5-1 shows normalised chord length probability distribution functions where each data point represents the probability of a bubble chord length in 0.5 mm intervals : e.g., the probability of a chord length from 1.0 to 1.5 mm is represented by the data point labelled 1.25. The probability of bubble chord lengths greater than 10 mm is not shown for clarity. In Figure 5-1, the measured bubble chord length distribution is the thick solid line and the thin dashed line is the estimated chord size distribution using Equation (5-1).

Fig. 5-1 - Bubble chord size distributions in the developing region of two-dimensional supported plunging jets: comparison between measured chord lengths and Equation (5-1)

(A) Definition sketch of vertical supported jets used by CHANSON and BRATTBERG (1996) and CUMMINGS and CHANSON (1997b)



(B) Measurements by CHANSON and BRATTBERG (1996) : x_1 = 0.100 mm, V_1 = 3.0 m/s, d_1 = 0.0106 m, x - x_1 = 0.050 m



(C) Measurements by CUMMINGS and CHANSON (1997b) : x_1 = 0.0875 mm, V_1 = 6.14 m/s, d_1 = 0.012 m, x - x_1 = 0.050 m

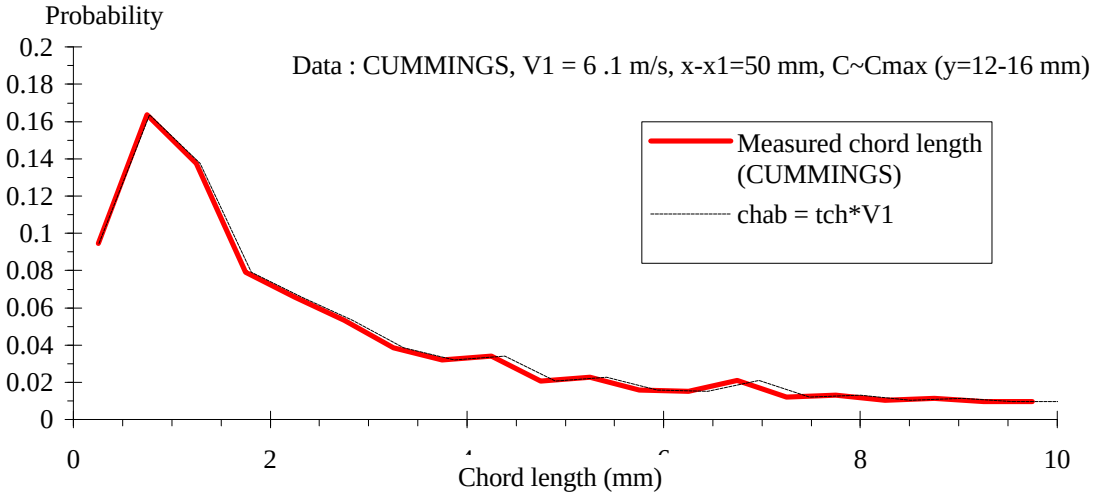


Figure 5-1 shows a wide range of entrained bubble sizes in plunging jet flows from less than 0.5 mm to more than 10 mm The distributions are skewed with a preponderance of small bubbles relative to the mean. In both examples, the probability of bubble chord length is the largest for bubble sizes between 0.5 and 1.0 mm. Figure 5-1 illustrates further that Equation (5-1) predicts accurately the shape of the probability distribution functions and that it overestimates bubble chord lengths by about 10 to 30%. (For the high-velocity experiment (Fig. 5-1C), it predicts bubble chord lengths within 5 to 10%, but it overestimates the chord sizes by about 30% in the lowest jet velocity experiment (Fig. 5-1B) which was associated with small bubble count rates (i.e. F < 50 Hz).)

In the following section, bubble chord times are presented in terms of the pseudo-chord length ch_{ab}. Although Equation (5-1) overestimates the bubbles size by 10 to 30%, the results are easier to comprehend and to compare with visual observations, high-speed photographs and movies.

5.2 Observations of bubble chord times

Some pseudo-bubble chord length distribution results are shown in Figure 5-2 and the complete data are reported in Appendix C. In Figure 5-2, each figure shows the normalised probability distribution function of pseudo-chord length ch_{ab} where the histogram columns represent the probability of chord length in 0.5 mm intervals : e.g., the probability of a chord length from 2.0 to 2.5 mm is represented by the column labelled 2.0. The last column (i.e. > 10) indicates the probability of chord lengths exceeding 10 mm. Each histogram describes all bubbles detected in a cross-section (i.e. 8 locations) at depths $(x - x_1)$ = 10, 15 and 25 mm.

For all water solutions and investigated inflow conditions, the data demonstrate the broad spectrum of pseudo-bubble chord lengths at each cross-section : i.e., from less than 0.5 mm to larger than 10 mm (Fig. 5-2). The pseudo-bubble chord length distributions are skewed with a preponderance of small bubble sizes relative to the mean. The probability of bubble chord length is the largest for bubble sizes between 0 and 2 mm although the mean pseudo-chord size is typically 4 to 6 mm (Table 5-1). It is worth noting the large fraction of bubbles larger than 10 mm next to the impingement perimeter : that is, for $(x-x_1)/r_1$ = 1.6 ($x-x_1$ = 10 mm, Fig. 5-2B, 5-2C & 5-2D). These large bubbles may be large air packets entrapped at impingement which are subsequently broken up by turbulent shear.

Discussion

Mean chord sizes and standard deviations of pseudo-chord sizes are summarised in Table 5-1. In Table 5-1, the number of samples is listed in column 5 while the mean and standard data are given in columns 6 and 7. The results highlight that the mean pseudo-chord sizes are between 3 and 7 mm. That is, there is predominance of millimetric entrained bubbles, even in seawater. The latter result contradicts suggestions that fine bubbles are predominant at breaking waves in the Sea.

At a given cross-section, the mean chord size increases with increasing jet velocity for a given water solution. The trend characterises the entrainment of larger air packets with increasing impact velocity V_1 and it is consistent with two-dimensional plunging jet observations (e.g. CUMMINGS and CHANSON 1997b).

Figure 5-3 shows comparative results obtained for identical inflow conditions (x_1/d_o = 4, Fr_1 = 9), three water solutions and two model sizes (for freshwater only). The black symbols are mean pseudo-chord sizes and the white symbols are standard deviations. (The smallest model data are the diamond symbols.) First the data show a decrease in mean chord size ch_{ab} with increasing distance from impingement (Fig. 5-3). The trend is consistent with the observations of CUMMINGS and CHANSON (1997b, 1999) and BRATTBERG and CHANSON (1998) in the developing flow region of two-dimensional plunging jet flows. Second mean pseudo-chord sizes were consistently the smallest in seawater and saltwater results were intermediate. Third mean chord sizes are consistently smaller in Model 3 than in the larger Model 2 for one set of identical inflow conditions (Fr_1 = 9, x_1/d_o = 4).

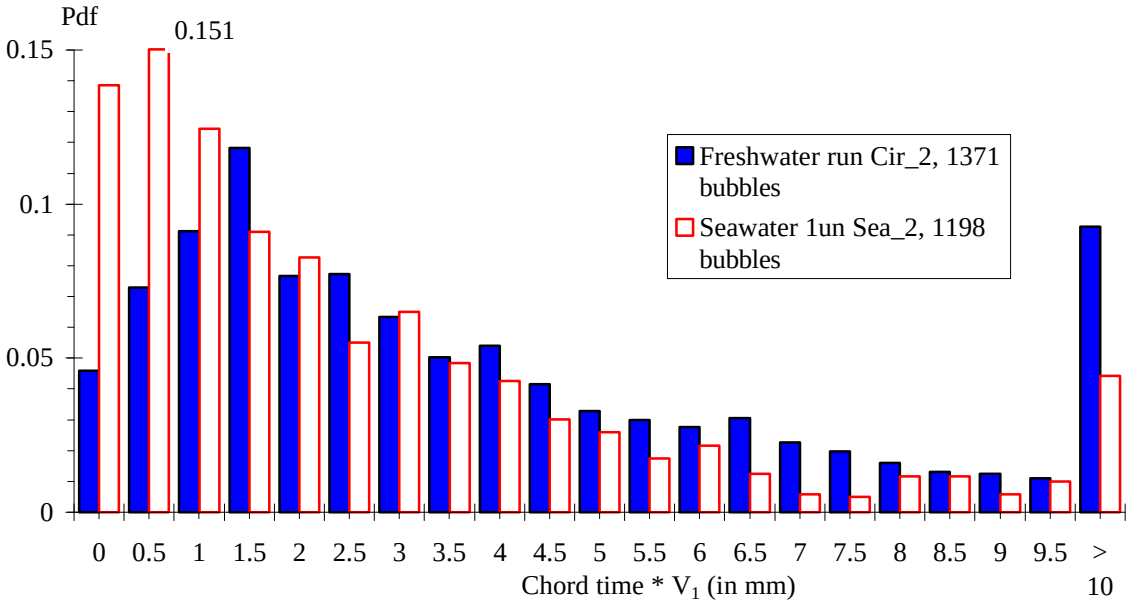
Table 5-1 - Measured means and standard deviations of pseudo chord length ch_{ab}

Run	V_1	Fr_1	$\frac{x-x_1}{r_1}$	Nb of bubbles	Mean ch_{ab}	Std ch_{ab}	Remarks
	m/s				mm	mm	
(1)	(2)	(3)	(4)	(5)	(6)	(7)	(8)
Model 2							Freshwater
Cir_2	2.42	7.07	4.19	1371	4.48	5.89	
Cir_4	3.04	8.81	4.11	2517	4.92	7.00	
Cir_5	3.18	9.20	1.64	2999	7.54	14.11	
			2.46	3341	5.79	10.78	
			4.10	2887	5.07	8.67	
Cir_6	3.46	9.98	4.09	3421	6.27	11.04	
Model 3							Freshwater.
Run_3	2.32	9.07	1.65	2058	3.83	7.78	
			2.47	1940	3.47	6.66	
			4.12	1660	3.36	5.98	
Model 4							Seawater
Sea_2	2.46	7.19	4.18	1198	3.08	4.58	
Sea_4	2.87	8.34	4.13	1947	3.90	8.31	
Sea_5	3.13	9.07	1.64	3787	5.56	13.40	
			2.46	3080	4.39	8.77	
			4.11	1859	4.29	8.20	
Sea_6	3.36	9.70	4.09	2823	4.58	9.18	
Model 5							Salty freshwater
Salt_5	3.12	9.04	1.64	3122	6.75	13.61	
			2.46	2561	4.50	7.56	
			4.11	2157	4.60	8.94	

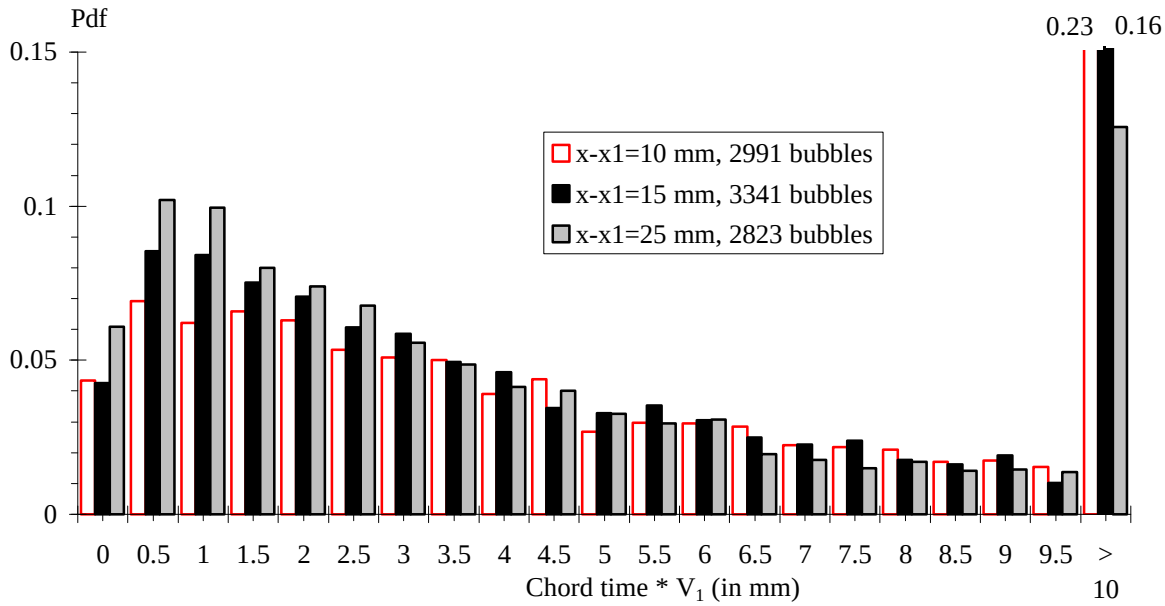
Notes : Nb of bubbles : number of samples (column 5); Mean ch_{ab} : mean pseudo-bubble chord length (column 6); Std ch_{ab} : standard deviation of pseudo-chord length (column 7).

Fig. 5-2 - Pseudo-bubble chord length distributions ($ch_{ab} = V_1 * t_{ch}$)

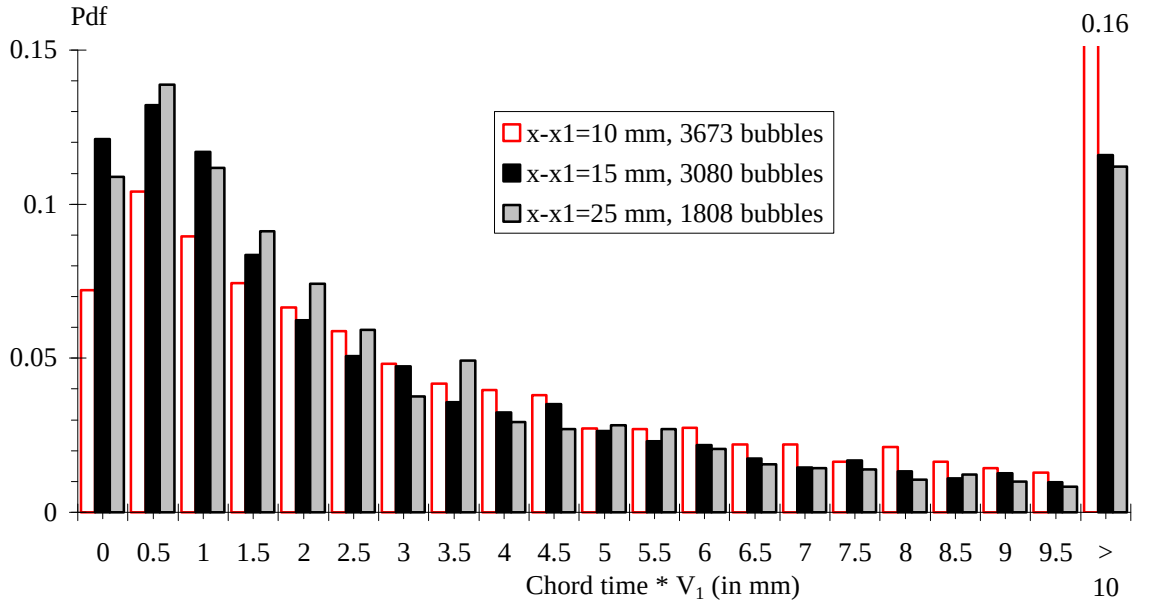
(A) $Fr_1 = 7$, $x_1/d_o = 4$, $(x-x_1)/r_1 = 4$: Model 2 (Freshwater, run Cir_2) and Model 4 (Seawater, run Sea_2)



(B) Fr_1 = 9.1, x_1/d_o = 4, Model 2 (Freshwater, run Cir_5)



(C) Fr_1 = 9.1, x_1/d_o = 4, Model 2 (Seawater, run Sea_5)



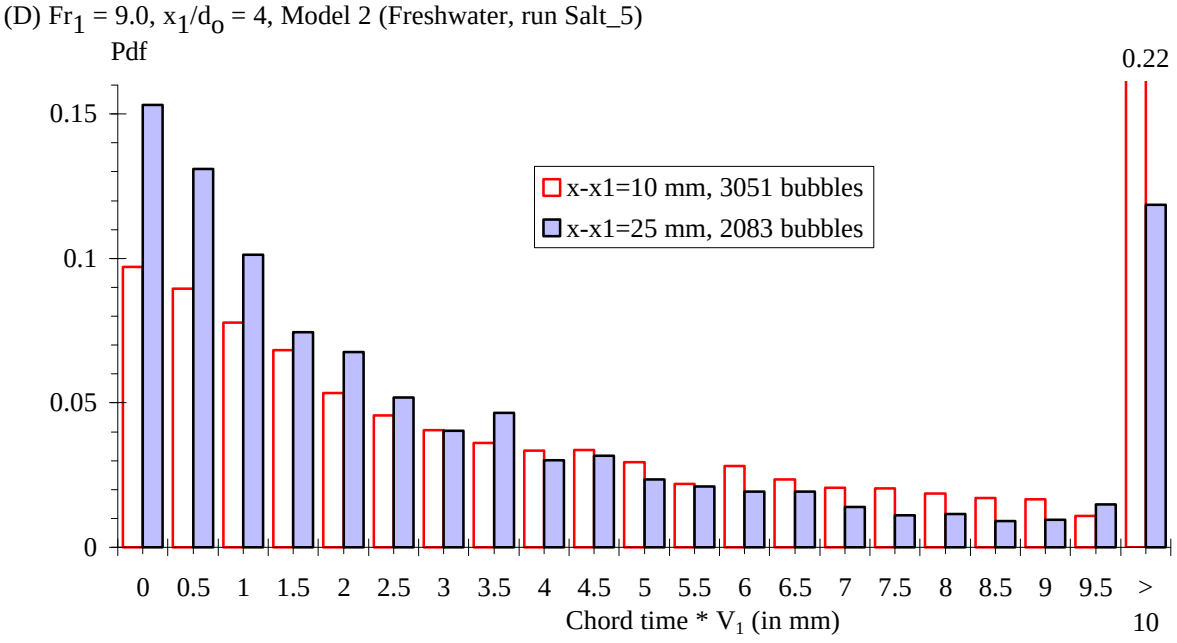
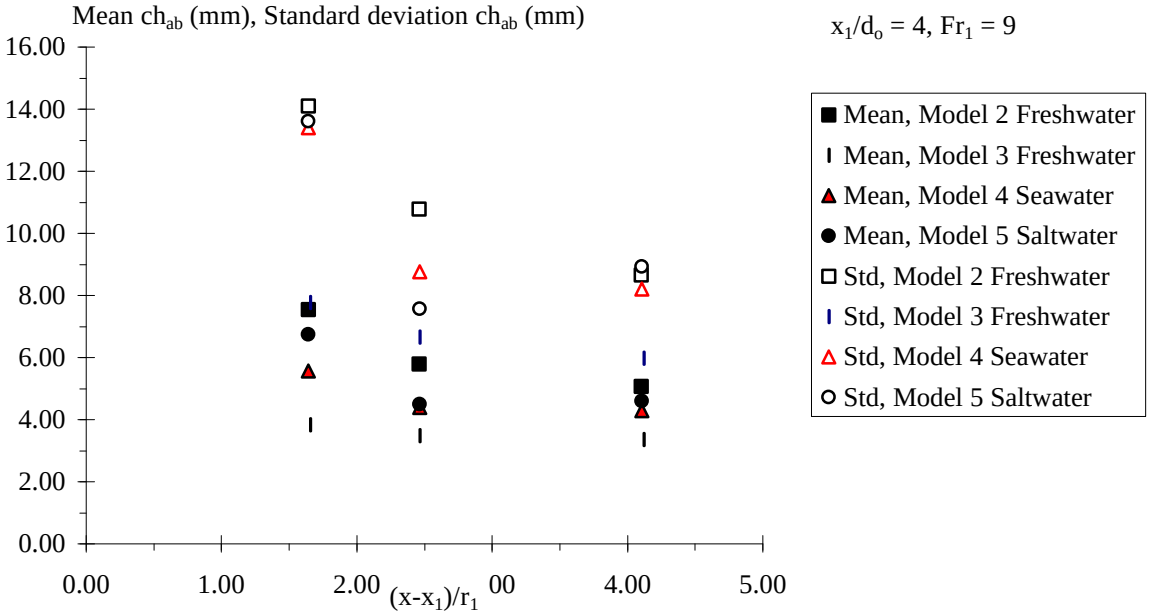


Fig. 5-3 - Mean and standard deviation of pseudo-bubble chord size for x_1/d_o = 4 and Fr_1 = 9 - Comparison between freshwater (Model 2), seawater (Model 4) and salty freshwater (Model 5) results



5.3 Comparison between different water solutions

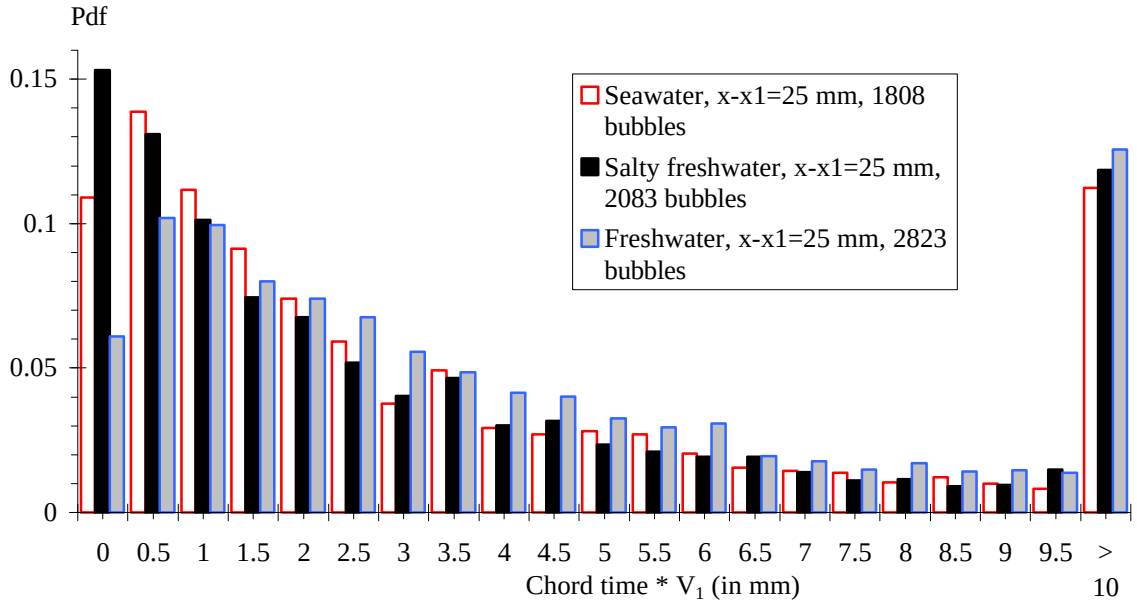
Figures 5-2B, 5-2C and 5-2D present pseudo-bubble chord length distributions for identical inflow conditions with different water solutions while Figure 5-4 shows comparative results at $(x-x_1)/r_1$ = 4. The experimental results show consistently several trends.

In seawater, the typical pseudo-bubble size is millimetric with mean chord sizes of about 3 to 6 mm. For example, 75% of entrained bubbles in seawater have a pseudo-chord length greater than 1 mm in Figure 5-4. Further seawater plunging jet flows contain, comparatively, a greater number of fine bubbles than freshwater

plunging jet flows for identical inflow conditions. This is caused possibly by the combination of lesser entrainment of large-size bubbles and greater entrapment of fine bubbles (in seawater).

Pseudo-chord size distributions in seawater and saltwater are reasonably close for identical inflow conditions and cross-section locations although, in salty freshwater, the probability of bubble chord lengths appears to be the largest for bubble sizes between 0 and 0.5 mm. A detailed analysis of probability distribution functions was conducted for pseudo-chord sizes between 0 and 2 mm with 0.1 and 0.2 mm intervals. The results showed that the probability of pseudo-chord length was the greatest between 0.1 and 1.2 mm in seawater and between 0.2 and 1.0 mm in salty freshwater. That is, the difference in bubble chord size distributions was small between seawater and saltwater, and the arbitrary choice of 0.5 mm intervals, as shown in Figure 5-4, may be misleading for small chord sizes between 0 and 1.5 mm.

Fig. 5-4 - Comparison of pseudo-bubble chord sizes for x_1/d_o = 4, Fr_1 = 9 and $(x-x_1)/r_1$ = 4 between freshwater (Model 2), seawater (Model 4) and salty freshwater (Model 5)



5.4 Comparison between two geometrically similar models

Figure 5-5 presents pseudo-bubble chord length distributions for identical inflow conditions with freshwater between Model 2 (d_o = 12.5 mm) and Model 3 (d_o = 6.8 mm). Figure 5-5A shows comparative results at $(x-x_1)/r_1$ = 1.65 and Figure 5-5B at $(x-x_1)/r_1$ = 4.1. The experimental results show consistently several trends.

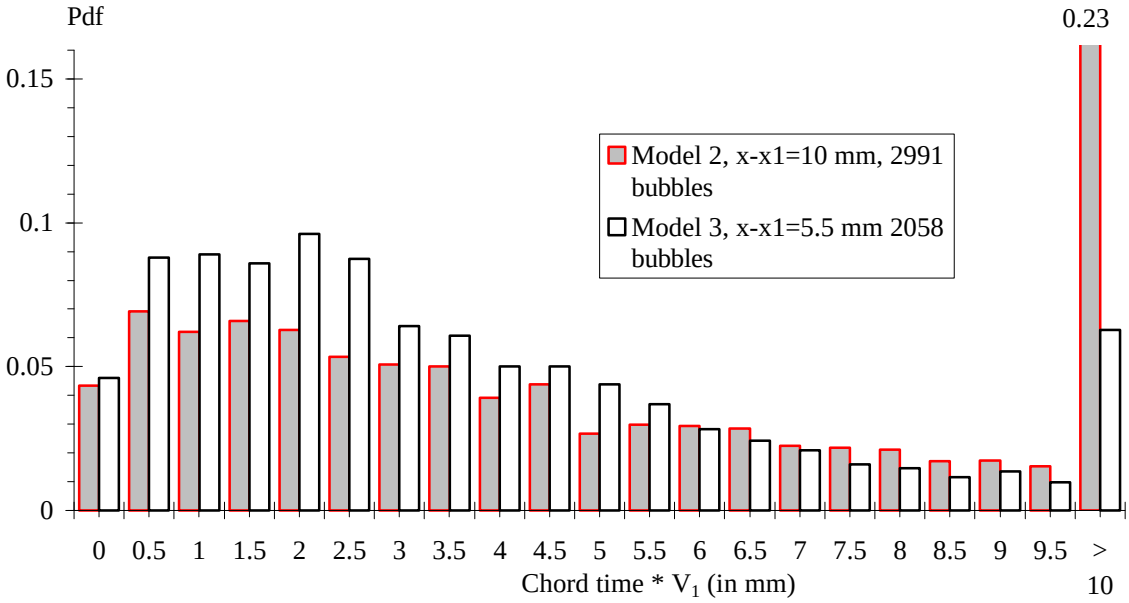
First, in the smallest model, the number of entrained bubbles with pseudo-chord size larger than 10 mm was basically negligible. The result is consistent with the observations of lesser void fraction in the smallest model for identical inflow conditions (e.g. Fig. 4-4).

Second, for chord sizes less than 10 mm, the mode was consistently smaller in the largest model (Model 2). For example, at (x-x)/r1 =1.65, the mode was about 0.5-2 mm in Model 2 and 0.5-3 mm in Model 3 (Fig. 5-5A). For pseudo-chord sizes less than 10 mm, the mean chord length was consistently 50 to 10% smaller in Model 2 than that in the smaller Model 3 at a similar cross-section.

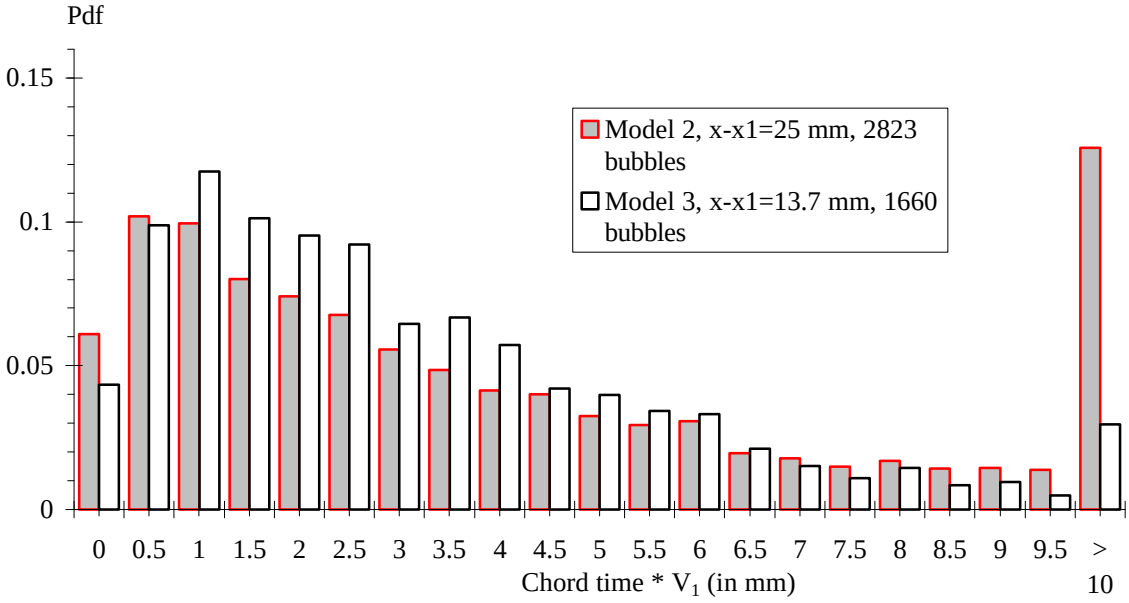
Overall the comparative results suggest a lesser entrainment of both large (ch_{ab} > 10 mm) and small (ch_{ab} < 1 mm) bubbles in the smallest Model 3.

Fig. 5-5 - Comparison of pseudo-bubble chord sizes for x_1/d_o = 4, Fr_1 = 9 between Model 2 (d_o = 12.5 mm) and Model 3 (d_o = 6.8 mm) with freshwater

(A) $(x-x_1)/r_1$ = 1.65



(B) $(x-x_1)/r_1$ = 4.1



6. DISCUSSION.

6.1 Scaling air entrainment at vertical circular plunging jets

Experiments were conducted with three geometric scales based upon a Froude similitude with undistorted geometric scale. For identical fluids in all three Models, the Froude similitude implies that the Weber number differs between experiments and that surface tension-dominated processes may not be properly scaled.

In the present study, identical results were observed for Fr_1 = 8.4 and 9.1 between Models 1 and 2 (freshwater solution). Some differences were noted for the lowest Froude number (Fr_1 = 7) : that is, a faster decay of void fraction and bubble count rate with distance $(x-x_1)/r_1$ in Model 2. The trend suggests a greater detrainment rate in Model 2 because the bubble rise velocity cannot be scaled properly with a Froude similitude. (The rise velocity was found to be nearly identical in all Models (App. A).) Based upon the present study, it is suggested that scale effects occur for $V_1/u_r < 10$ in vertical circular plunging jets, where u_r is the characteristic rise velocity of entrained air bubbles.

Model 3 data showed consistently less entrained air than the two larger models : that is, lesser void fractions and dimensionless bubble count rates for identical inflow conditions. The observations imply that all experiments in the smallest model were affected by scale effects and that the rate of air entrainment was underestimated in Model 3. For the range of investigated flow conditions (Table 2-1), air entrainment at vertical circular jets was affected by scale effects for $We_1 < 1000$ where We_1 is the inflow Weber number.

6.2 Air entrainment at plunging breaking waves

The present results may be applied to air entrainment at plunging breaking waves (Fig. 6-1).

Laboratory studies of breaking waves may be affected by scale effects in terms of air entrainment when the jet impact conditions satisfy $We_1 < 1000$ where We_1 is the Weber number at impact (paragraph 6.1). At plunging breakers, the jet impact velocity may be roughly estimated as $\sqrt{2*g*H_b}$ and the jet thickness is approximately $0.05*H_b$ where H_b is the wave crest elevation at breaking measured above still water level (CHANSON and CUMMINGS 1994a). This yields scale effects in laboratory for $H_b < 0.25$ m ([8]). That is, laboratory studies of wave breaking underestimate air entrainment when the wave height at breaking is less than 0.25 to 0.35 m ([9]). Such a condition is restrictive. Figure 6-2 illustrates a comparison between small prototype plunging breakers and a laboratory study. In the latter, H_b was about 0.1 m and the first writer observed comparatively lesser entrained air than in prototype. Note, however, that the present study was conducted with vertical circular jets, while, at plunging breakers, the plunging jet is quasi two-dimensional and inclined to about 30 degrees with the receiving surface (CHANSON and LEE 1997). More, it is an unsteady process ([10]).

---

[8]Note that, for $H_b < 0.25$ m, the ratio of jet impact velocity to bubble rise velocity is smaller than 10 and the detrainment rate in laboratory is not scaled properly : i.e., it will greater than in prototype.

[9]For the experiments of CHANSON and LEE (1997), the ratio of wave crest elevation at breaking measured above still water level H_b to breaking wave height was 0.75 in average.

[10]CHANSON et al. (1999) studied qualitatively air entrainment at unsteady plunging jets with jet impact velocities ranging from 4.8 to 6.1 m/s and jet durations between 5 and 12 s.

Fig. 6-1 -Sketch of a plunging breaker

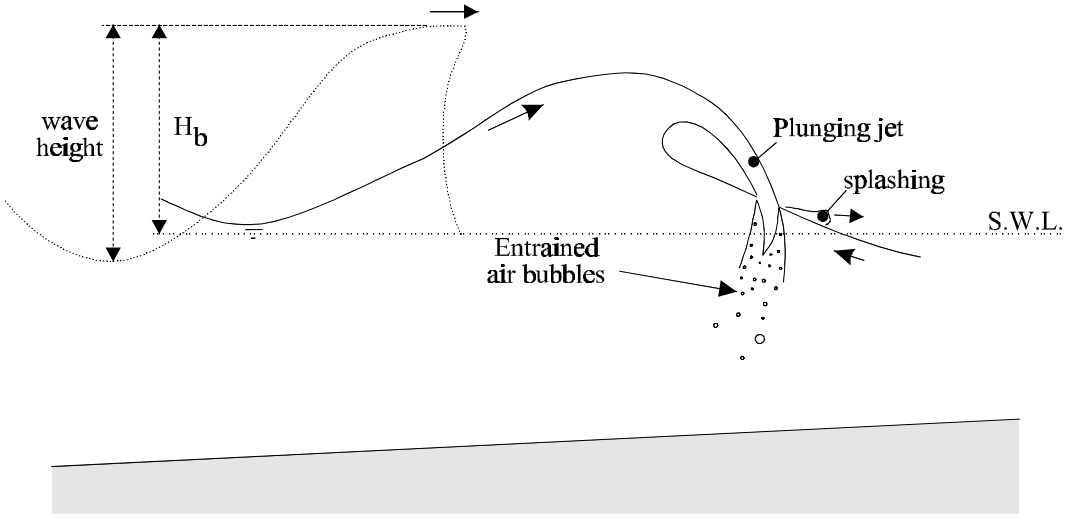


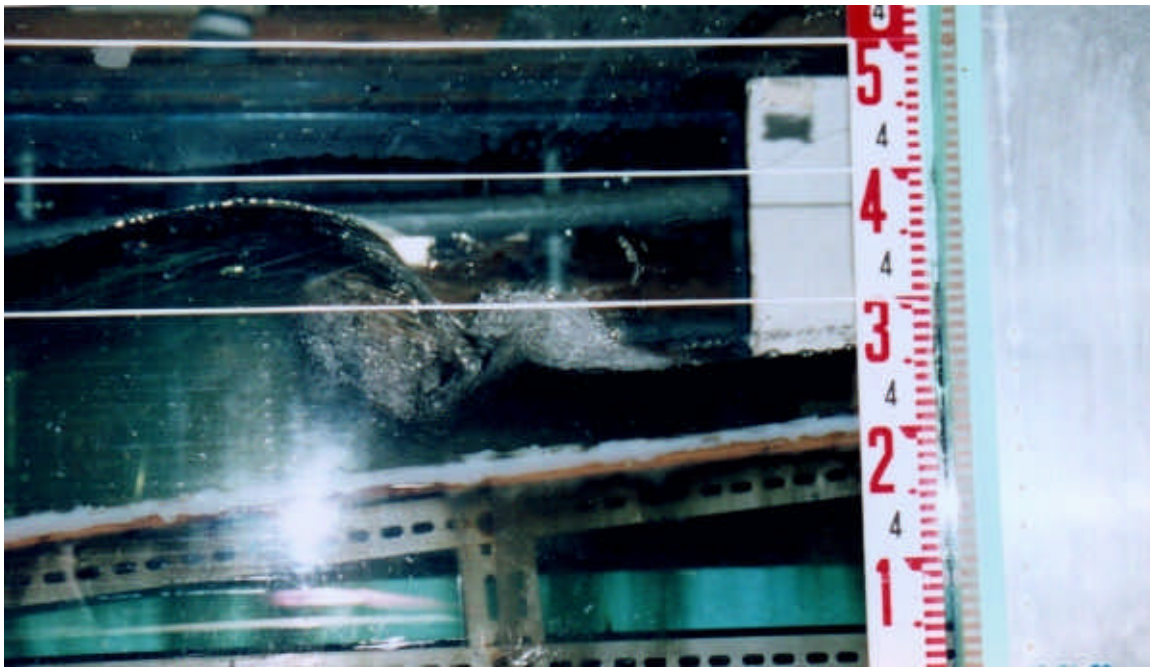
Fig. 6-2 - Comparison of air entrainment in prototype and in laboratory

(A) Plunging breaker at Terasawa beach on 23 Nov. 2001 at high tide



(B) Laboratory model of a plunging breaker on a sloping beach

Water depth : 0.5 m, beach slope: 1V:6H



In artificial reservoirs, it is common practice to estimate the wave climate based upon coastal observations (e.g. USBR 1987). For an identical wave climate, however, plunging breaking waves in freshwater lakes will entrain greater amounts of air than in seawater. They will contribute to greater air-water mass transfer rate than in seawater and saltwater. On the other hand, relatively more small entrained bubbles are observed in seawater. Such bubbles have a longer residence time in seawater. First they have a smaller bubble rise velocity (App. A) than identical bubbles in freshwater. Second bubbles with small rise velocities have a greater susceptibility to be trapped in vortical structures during the ascent. In turn, their "real" rise time may be greatly increased ([11]), and mass transfer is enhanced.

In the present study, the physical properties of water that were considered in the dimensional analysis (paragraph 1.4) were the density, viscosity and surface tension. For the investigated water solutions, the differences in water properties were small (Table 2-2) and they cannot explain nor justify the drastic reduction in air entrainment observed in seawater. It is believed that Equation (1-3) is incomplete and that air entrainment at plunging jets is affected by further physical, chemical and biological properties.

A comparison between seawater and saltwater experimental results shows further greater air entrainment in salty freshwater than in seawater. This may suggest some difference in air entrainment process which cannot be explained by differences in salinity nor conductivity, but which might be related to different chemical ([12]) and biological properties : e.g., effect of plankton ! The role of living organisms (e.g. plankton) cannot be ignored.

---

[11]CHANSON (1997) reviewed the effects of turbulence on the rise velocity. Most studies suggested that high-level of turbulence would retard the bubble rise resulting in smaller rise velocities than in still water.

[12]Appendix D describes the saltwater and seawater compositions.

For example, phytoplankton, with plant cells ranging in sizes from 1 to few hundreds microns, might interact with microscale turbulence and bubbles, and inhibit some bubble entrainment; zooplankton which are greater than 0.05 mm in size might interact with small scale turbulent eddies and small-size bubbles, in a similar fashion as stretched molecules of dilute polymers.

7. CONCLUSION

Air entrainment and bubble dispersion at vertical circular plunging jets were investigated for a range of flow conditions and water solutions (Table 6-1). The project was focused on scale effects affecting air entrainment and bubble dispersion at vertical circular plunging jets, and a comparative study of air entrainment in freshwater and in seawater. Three scale models were used with jet nozzle diameters of 6.8, 12.5 and 25 mm. Experiments were performed with three water solutions : freshwater (tap water), salty freshwater and seawater (Table 6-2). Detailed air-water measurement were performed systematically based upon a Froude similitude. All experimental results are presented in Appendices B and C.

Basic results may be summarised as follow :

1- A study of air entrainment inception conditions shows that the inception velocity V_e is identical for freshwater, seawater and salty freshwater for one experiment.

2- For jet velocities greater than the onset velocity (i.e. $V_1 > V_e$), the distributions of void fraction in the developing flow region follow closely an analytical solution of the advection diffusion equation for air bubbles (i.e. Eq. (4-2)).

3- In freshwater, the results highlight significant scale effects when $We_1 < 1000$ or $V_1/u_r < 10$, where We_1 is the inflow Weber number, V_1 is the jet impact velocity and u_r is the bubble rise velocity. For $We_1 < 1000$, the air entrainment rate is underestimated. For $V_1/u_r < 10$, the detrainment rate is overestimated.

4- In seawater, significantly less air is entrained than in freshwater, all inflow parameters being equal. The writers hypothesise that surfactants, biological and chemical elements harden the induction trumpet and diminish air entrapment at impingement in seawater (Fig. 1-3). Air entrainment rates in saltwater are intermediate between seawater and freshwater results.

5- The mean pseudo-chord sizes were between 4 and 6 mm for all water solutions, where the pseudo-bubble chord length $ch_{ab} = V_1 * t_{ch}$ was found to overestimate real bubble chords by 10 to 30%.

6- Distributions of pseudo-bubble chord sizes ranged from less than 0.5 mm to more than 10 mm for all water solutions.

7- Comparatively, however, more fine bubbles were detected in seawater than in freshwater. Such fine bubbles (less than 0.5 mm) have a slower rise velocity and their underwater residence time is larger in seawater. They give a visual, misleading appearance to the air-water flow suggesting inaccurately that very fine bubbles are predominantly entrained in seawater plunging jets.

8- Air entrainment at plunging jets in saltwater and seawater differs : i.e., less air and smaller bubbles are entrained in seawater. The results imply that classical dimensional analysis (e.g. paragraph 1.4) is incomplete and that air entrainment at plunging jets is affected by physical, chemical and biological properties other than density, viscosity and surface tension.

9- In laboratory wave flumes, air entrainment at plunging breaking waves is affected by scale effects when the wave height at breaking is less than 0.25 to 0.35 m.

10- In one series of experiments ($Fr_1 = 9$) performed with $d_o = 6.8$ and 12.5 mm, the results suggest a lesser entrainment of both large ($ch_{ab} > 10$ mm) and small ($ch_{ab} < 1$ mm) bubbles in the smallest Model 3.

Overall the study demonstrates that air entrainment in the Sea is a complicated process which cannot be modelled accurately in small-size wave flumes nor with fresh water experiments. It is hypothesised that living organisms in seawater might play a role in inhibiting bubble entrainment and this aspect must be investigated systematically under controlled flow conditions. Further studies of air-water plunging jet flows should also investigate air-water velocity distributions and turbulent velocity fluctuations.

Table 6-1- Summary of experimental investigations

Ref.	d_o m	x_1 m	V_1 m/s	Fr_1 m	Comments
(1)	(2)	(3)	(4)	(5)	(6)
Model 1	0.025	0.1	3.5	7.2	Freshwater (tap water, σ = 0.055 N/m). Vertical jet. Inflow pipe: 3.5 m long, 0.054 m diameter. Water depth: ~1.5 m.
			4.1	8.4	
			4.4	9.0	
Model 2	0.0125	0.05	2.42	7.1	Freshwater (tap water, σ = 0.073 N/m). Vertical jet. Inflow pipe: 1.2 m long, 0.0125 m diameter. Water depth: ~0.65 m.
			3.04	8.8	
			3.18	9.2	
			3.46	10.0	
Model 3	0.00683	0.0273	1.79	7.1	Freshwater (tap water, σ = 0.073 N/m). Vertical jet. Inflow pipe: 1 m long, 0.00683 m diameter. Water depth: ~0.65 m.
			2.16	8.5	
			2.30	9.0	
			2.49	9.7	
Model 4	0.0125	0.05	2.46	7.2	Seawater (Pacific Ocean, σ = 0.076 N/m). Vertical jet. Inflow pipe: 1.2 m long, 0.0125 m diameter. Water depth: ~0.65 m.
			2.87	8.3	
				9.1	
			3.13	9.7	
			3.36		
Model 5	0.0125	0.05	3.12	9.0	Freshwater with 34.5 ppt NaCl (99.5% quality) (σ = 0.075 N/m). Vertical jet. Inflow pipe: 1.2 m long, 0.0125 m diameter. Water depth: ~0.65 m.

Note : σ : measured surface tension between air and water.

Table 6-2- Summary of water solution properties

Property	Tap water	Seawater	Salty tap water (3.45% solution)	Remarks
(1)	(2)	(3)	(4)	(5)
Experiments :	Models 1, 2 & 3	Model 4	Model 5	See Table 6-1.
Density (kg/m^3) :	998.2	1,024	1,024	At 20 Celsius.
Dynamic viscosity (Pa.s):	1.015 E-3	1.22 E-3	1.18 E-3	At 20 Celsius.
Kinematic viscosity (m^2/s):	0.925 E-6	0.971 E-6	0.962 E-6	At room temperature (about 22 Celsius).
Surface tension (N/m):	0.075 (Models 2 & 3) 0.055 (Model 1)	0.076	0.075	At room temperature (about 22 Celsius).
Conductivity (µS/cm):	87.7	48,500 49,100	53,600	At 25 Celsius.

ACKNOWLEDGMENTS

The authors acknowledge the financial support of the Australian Academy of Science, Japan Society for the Promotion of Science and Ministry of Education, Culture, Sports, Science and Technology, Japan. H. CHANSON and S. AOKI thank their students for assistance, especially : T. McGIBBON and B. BOLDEN (Australia), Mr IWATA and Ms KIDA (Japan). They acknowledge the helpful comments of Dr T. SUZUKI (T.U.T.), Dr YAMADA (T.U.T.), Dr Y. YASUDA (Nihon University), Dr R. MANASSEH (C.S.I.R.O.). The writers thank the group of graduates students, including the surfers, who assisted in collecting "fresh" seawater off the Enshu coast.